

PROGRESS IN ATOMIC FORCE MICROSCOPY

Habilitationsschrift

für das Fach Experimentalphysik
der Mathematisch-Naturwissenschaftlichen Fakultät
der Universität Augsburg

vorgelegt von

Dr. rer. nat. Franz J. Gießibl

Augsburg

November 2000

Acknowledgements

Thanks to Birgit and Severin for their love and support!

Jochen Mannhart has given me the opportunity to work on experimental and theoretical aspects of AFM at the Lehrstuhl für Experimentalphysik VI at Augsburg University. He has supported our project with great spirit and was enthusiastically engaged in planning and interpreting our experiments. Special thanks to all members of the scanning probe microscopy group for their contributions: Hartmut Bielefeldt, Stefan Hembacher, Ulrich Mair and Thomas Ottenthal. Klaus Wiedenmann helped in the construction of the AFM/STM and the machine shop with Stefan Werner and coworkers did great work in the machining of intricate parts. Hans Hilgenkamp and Darrell Schlom were deeply engaged in fruitful discussions about the physics of AFM. Thanks also to Felicitas Samtleben-Spleiss and Eleonore Saladie for helping with administrative issues and thanks to the Bundesministerium für Bildung und Forschung for funding our research project.

Alexis Baratoff, Urs Dürig and Peter van Dongen contributed fruitful discussions in the theoretical analysis of frequency shifts and in modeling of the tip-sample force.

Lukas Howald and Dominik Müller from Nanosurf AG helped to optimize the qPlus sensor and supplied us with an ultrastable phase-locked-loop detector which has been instrumental for the achievement of our best experimental results.

McKinsey&Company has supported the first steps of the creation of the qPlus sensor.

During my graduate and postgraduate work at the IBM Physics Group Munich from 1988 until 1992 Gerd Binnig taught me the first things about AFM and his unusual approach to solve experimental problems and Christoph Gerber shared his mastership in implementing instrumentation. Calvin Quate has had a continuous interest in the improvement of the resolution of the AFM and has contributed ongoing fruitful discussions and hints to collaborators and important literature.

Brian Trafas, Marco Tortonese, Stuart Presley, Mike Kirk, Sang-il Park and Tom Albrecht made it great fun to work in Silicon Valley.

Hartmut Bielefeldt, Van Eden and Stefan Hembacher have helped in proofreading the manuscript and German Hammerl, Stefan Hembacher and Ralf Bulla have provided

support in L^AT_EX.

Contents

1	Introduction	3
2	Principles of operation	7
2.1	Scanning Tunneling Microscope (STM)	7
2.1.1	Imaging signal in STM	9
2.1.2	Experimental measurement and noise	10
2.2	Atomic Force Microscope (AFM)	13
2.2.1	Imaging signal in AFM	13
2.2.2	Experimental measurement and noise	15
2.3	Operating Modes of AFMs	17
2.3.1	Static AFM	17
2.3.2	Dynamic AFM	18
3	The four additional challenges faced by AFM	21
3.1	Jump-to-contact problem	22
3.2	Non-monotonic imaging signal	22
3.3	Contribution of long-range forces	23
3.4	Noise in the imaging signal	23
4	Frequency-modulation AFM (FM-AFM)	25

4.1	Experimental setup	25
4.2	Applications	29
5	Calculation of the frequency shift in FM-AFM	33
5.1	Generic calculation	33
5.1.1	Hamilton-Jacobi Method	34
5.1.2	Fourier Method	35
5.1.3	A very simple expression for frequency shifts as a function of the tip-sample forces	36
5.2	Frequency shift for a typical tip-sample force	37
5.3	Calculation of the tunneling current for oscillating tips	39
6	Noise in frequency modulation AFM	41
6.1	Generic calculation	41
6.2	Noise in the frequency measurement	42
6.2.1	Fluctuations of the cantilever deflection	42
6.2.2	Drifts of the eigenfrequency	45
6.3	Optimal amplitude for minimal vertical noise	46
7	A novel force sensor based on a quartz tuning fork	47
7.1	Quartz versus silicon as a cantilever material	47
7.2	Previous applications of tuning forks in scanning probe microscopy	48
7.3	Benefit of clamping one of the beams (qPlus configuration)	49
8	Summary and Outlook	51
9	Bibliography	55
10	Appendix: Selection of previously published work	63

Chapter 1

Introduction

The invention of the Scanning Tunneling Microscope (STM) in 1981 [18] has provided a breakthrough in our possibilities to investigate matter on the atomic scale: for the first time, the individual surface atoms of flat samples could be made visible in real space. Only one year after its invention, one of the most intriguing problems in surface science was solved with the help of STM: the structure of the surface reconstruction of silicon (111)-(7x7) [19]. Gerd Binnig and Heinrich Rohrer, the inventors of the STM were rewarded with the physics Nobel prize in 1986, jointly with Ernst Ruska, the inventor of the Scanning Electron Microscope. The spectacular spatial resolution of the STM along with its elegant simplicity has helped to rapidly spread its use across the surface science community. A large number of metals and semiconductors have been investigated on the atomic scale and stunning images of the world of atoms have been created within the first few years after the inception of the STM. Some results have even fascinated the general public, e.g. the work of Eigler *et al.* where the STM was used to arrange individual atoms into letters only a few nanometers across [33]. In more recent experiments quantum structures have been formed from single atoms with an STM [27, 70].

The STM can only image electrically conductive samples which limits its application to imaging metals and semiconductors. But even conductors – except for a few special materials, like highly oriented pyrolytic graphite (HOPG) – cannot be studied in ambient conditions by STM but have to be investigated in an ultra-high vacuum in order to be able to prepare clean surfaces. This limitation was lifted in 1985 when Binnig, Quate and Gerber introduced the atomic force microscope (AFM) [21]. Like in the STM, a sharp tip is brought close to a sample, but rather than applying a bias

voltage and measuring the tunneling current, the force between tip and sample is measured. Because electrical conductivity of the sample is not required in AFM, the AFM can image virtually any flat solid surface. Consequently, thousands of AFMs are in use in universities, public and industrial research laboratories all over the world. However, the most of these instruments are operated in ambient conditions, where surfaces are covered with contamination layers and the atomic configuration changes constantly with adsorbing and desorbing atoms and molecules. For studying surfaces on the atomic level, an ultra-high vacuum environment is required, where it is more difficult to operate an AFM. While the inventors of AFM have anticipated true atomic resolution capability, it has taken almost a decade to achieve this feat. In addition to the requirements for performing STM with atomic resolution, AFM poses several additional challenges which are summarized in chapter 3. True atomic resolution with static AFM on inert samples was reported in the early nineties [37], [74]. However, imaging reactive surfaces like Si (111) in ultra-high vacuum by static AFM has shown that chemical bonding between the tip and sample and wear on the atomic scale prevents achieving true atomic resolution on silicon by AFM [53, 54].

The topic of this work is the establishment and improvement of AFM as a tool for surface science with a focus on true atomic resolution. Surface science requires experiments to be performed in an ultra-high vacuum. In 1994, true atomic resolution was first achieved on the Si(111)-(7×7) surface by this author [A2] with frequency modulation AFM (FM-AFM) [4]. In this experiment, a cantilever with a spring constant of $k = 17 \text{ N/m}$ was oscillating with an amplitude $A = 340 \text{ \AA}$, and the frequency shift caused by the tip-sample forces was used as the imaging signal. This result was confirmed soon after by several other groups using similar experimental parameters [61, 48, 69]. Other semiconductors [96], ionic crystals [77, 13, 83], metal oxides [35, 82], metals [68, 76], organic monolayers [44] and even a film of Xenon physisorbed on graphite [6] have been imaged with atomic resolution. In 1998, the “First International Workshop on Non-contact Atomic Force Microscopy (NC-AFM)” was held in Osaka, Japan with about 80 attendants. This meeting was followed by the second meeting in Pontresina, Switzerland in 1999 with roughly 120 participants and the third meeting in Hamburg, Germany in 2000 with more than 200 participants. The fourth meeting is scheduled for September 2001 in Kyoto, Japan, and the 2002 conference will take place in Santiago de Compostela, Spain.

While FM-AFM is a well established experimental technique, even more fascinating applications and results are expected in the future. Recently, subatomic resolution was demonstrated by AFM [A9], i.e. the spatial resolution of AFM is now surpassing that of STM. AFM yields information about the strength and geometry of single chemical bonds. Despite substantial progress, the experimental techniques are still improving, and stimulating challenges remain.

This text is structured in the following fashion: Chapter 2 contains a brief review of STM with a discussion of the driving factors which are the basis for the spatial resolution of STM and a comparison with the AFM. Chapter 3 summarizes the extra challenges which are faced by AFM in addition to the conditions for the successful operation of an STM. Chapter 4 describes the experimental implementation of FM-AFM in detail. Chapter 5 shows the calculation of the imaging signal, the frequency shift, as a function of the tip-sample forces and chapter 6 contains a calculation of the vertical noise as a function of the operating parameters. A new force sensor with properties which are close to the optimal sensor properties calculated in chapter 6 is described in chapter 7. A summary and outlook is given in chapter 8 and the bibliography, ordered alphabetically by the last name of the first author, is in chapter 9. A selection of 11 articles written by this author pertinent to the topics presented in chapters 2 - 7 are printed in the appendix. The citations of these articles are marked with a prefix 'A'.

Chapter 2

Principles of operation

2.1 Scanning Tunneling Microscope (STM)

Even though the principle of STM is explained very well in many excellent books and review articles [20, 22, 24, 45, 95, 108, 109], a brief review about STM is included here because the STM and AFM share many key features, and the additional challenges faced by AFM show up clearly in a direct comparison. Figure 2.1 shows

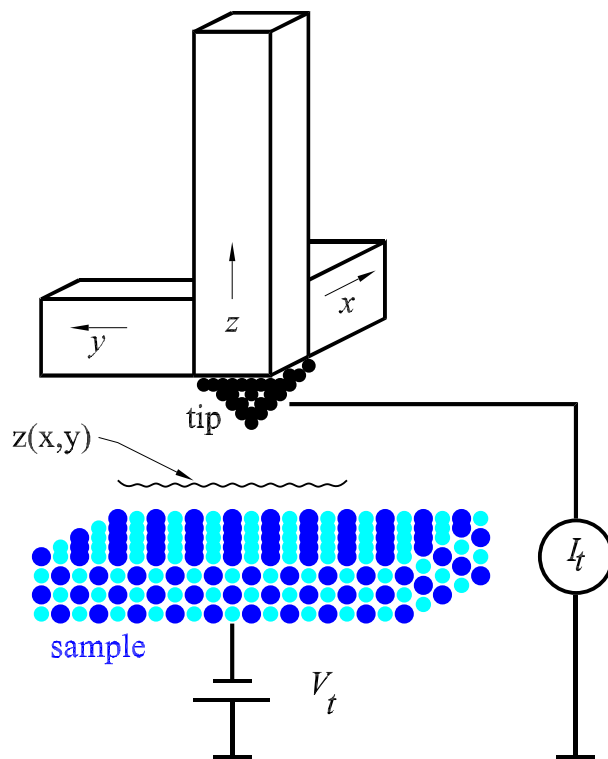


Figure 2.1: Schematic setup of a scanning tunneling microscope.

the general setup of a scanning tunneling microscope (STM): a sharp tip is mounted on a scanning device (“xyz scanner”) which allows 3-dimensional positioning in x , y and z with subatomic precision. The tunneling tip is typically a wire that has been sharpened by chemical etching or mechanical grinding. W, Pt-Ir or pure Ir are often chosen as a tip material. A bias voltage V_t is applied to the sample and when the distance between tip and sample is in the range of several Ångströms, a tunneling current I_t flows between the tip and sample. This current is used as the feedback signal in a z -feedback loop. The sample is mounted on a coarse positioning device used to bring the sample within the scanning range of the xyz scanner. Either the probe or sample can be mounted on the xyz scanner: the choice is entirely determined by practical considerations. Usually, the object that is lighter is mounted on the xyz scanner. In some SPMs, the xyz scanner is attached to the coarse positioning device. For obtaining atomic resolution, the mechanical loop consisting of probe, sample, xyz scanner and coarse positioning device needs to be stable enough such that ambient noise and other mechanical vibrations do not cause the relative position of the probe and sample to vary by more than a fraction of the diameter of an atom. This is usually achieved by a mechanically rigid design and a vibration isolation stage, which decouples the microscope from sound and other mechanical vibrations.

The approach of the sample and probe is typically monitored by an optical microscope. When the probe and sample are within a distance of a few micrometers, an automatic approach is engaged which brings the probe and sample into contact. A feedback loop adjusts z such that the magnitude of the imaging signal matches its setpoint. In the “topographic mode”, images are created by scanning the surface in the xy plane and recording the z position required to keep the imaging signal at the probe constant. In the “constant height mode”, the probe is scanned rapidly such that the feedback cannot follow the atomic corrugations. The atoms are then apparent as modulations of the imaging signal which is recorded as a function of x and y . The scanning is usually performed in a raster fashion with a fast scanning direction (sawtooth or sinusoidal signal) and a slow scanning direction (sawtooth signal). A computer controls the scanning of the surface in the xy plane while recording the z position of the tip (topographic mode) or the imaging signal (constant height mode). Thus, a three dimensional image $z(x, y)$ is created.

Instead of the tunneling tip, a force-sensing cantilever, an optical near-field probe, a microthermometer etc. can be mounted to the scanner, giving rise to a whole family of scanning probe microscopes [106].

2.1.1 Imaging signal in STM

In an STM, a sharp tip is brought close to an electrically conductive surface that is biased at a voltage V_t . When the separation is close enough, a current I_t flows between them. The typical distance between tip and sample under these conditions is a few atomic diameters, and the transport of electrons occurs by tunneling. When $|V_t|$ is

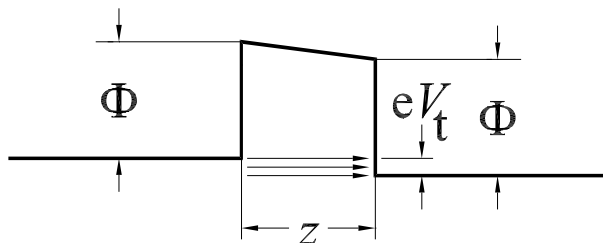


Figure 2.2: Energy diagram of an idealized tunneling gap.

small compared to the workfunction Φ , the tunneling barrier is roughly rectangular (see Fig.2.2) with a width z and a height given by the workfunction Φ . According to elementary quantum mechanics, the tunneling current is given by:

$$I_t(z) = I_0 e^{-2\kappa_t z}. \quad (2.1)$$

I_0 is a function of the applied voltage and the density of states in both tip and sample and

$$\kappa_t = \sqrt{2m\Phi}/\hbar \quad (2.2)$$

where m is the mass of the electron and \hbar is Planck's constant. For metals, $\Phi \approx 4 \text{ eV}$, thus $\kappa_t \approx 1 \text{ \AA}^{-1}$. When z is increased by one Ångström, the current drops by an order of magnitude. This strong distance dependence is the key reason for atomic resolution with an STM. Most of the tunneling current is carried by the atom that is closest to the sample ("front atom"). If the sample is very flat, this front atom remains the atom that is closest to the sample during scanning in x and y and even relatively blunt tips yield atomic resolution easily.

2.1.2 Experimental measurement and noise

The tunneling current is measured with a current-to-voltage converter (see Fig. 2.3), which is usually built with a single operational amplifier (OPA) with low noise and low input bias current, and a feedback resistor with a typical impedance of $R = 100 \text{ M}\Omega$. The tunneling current I_t is used to measure the distance between tip and

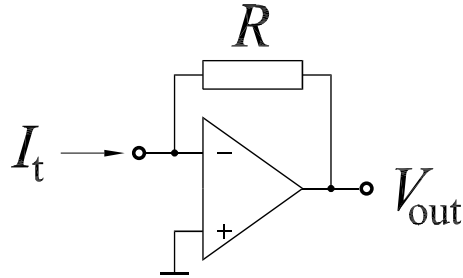


Figure 2.3: Current-to-voltage converter for an STM. The output voltage is given by $V_{out} = -R \times I_t$.

sample. The noise in the imaging signal (tunneling current in the case of STM, force or some derived quantity in the case of AFM) needs to be small enough such that the corresponding vertical noise δz is considerably smaller than the atomic corrugation of the sample. In the following, the noise levels for imaging signals and vertical positions are described by the root-mean-square (rms) deviation of the mean value and indicated by the prefix δ , i.e.

$$\delta\xi \equiv \sqrt{\langle (\xi - \langle \xi \rangle)^2 \rangle}. \quad (2.3)$$

For achieving atomic resolution with an STM or AFM, a first necessary condition is that the mechanical vibrations between tip and sample are smaller than the atomic corrugations. This condition is met by a microscope design emphasizing utmost stability and establishing proper vibration isolation, as described in Refs. [24, 95]. In the following, proper mechanical design and vibration isolation will be presumed and not discussed further. The inherent vertical noise in an STM is connected to the noise in the current measurement. Figure 2.4 shows the qualitative dependence of the tunneling current I_t as a function of vertical distance z . Because the measurement of I_t is subject to noise, the vertical distance measurement is also subject to a noise

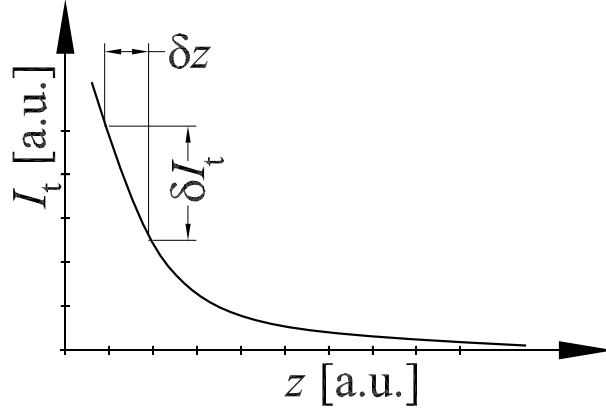


Figure 2.4: Tunneling current as a function of distance and relation between current noise δI_t and vertical noise δz (arbitrary units).

level δz :

$$\delta z_{I_t} = \frac{\delta I_t}{\left| \frac{\partial I_t}{\partial z} \right|}. \quad (2.4)$$

It is shown below, that the noise in the current measurement δI_t is small and that $\frac{\partial I_t}{\partial z}$ is quite large, consequently the vertical noise in STM is very small.

The dominating noise source in the tunneling current is the Johnson noise of both the feedback resistor R in the current amplifier, the Johnson noise in the tunneling junction, and the input noise of the operational amplifier. The Johnson noise density of a resistor R at temperature T is given by [52]:

$$n_R = \sqrt{4k_B T R} \quad (2.5)$$

where k_B is the Boltzmann constant. In typical STMs, the tunneling current is of the order of $I_t \approx 100$ pA and measured with an acquisition bandwidth of $B \approx 1$ kHz. With a gain of $V/I = R = 100$ M Ω and $T = 300$ K, the rms voltage noise is $n_i \sqrt{B} = \sqrt{4k_B T R B} = 40 \mu V$ at room temperature, corresponding to a current noise of $\delta I_t = 0.4$ pA. With Eqs. 2.1 and 2.4, the vertical noise is

$$\delta z_{I_t} \approx \frac{\sqrt{4k_B T B / R}}{2\kappa_t |I_t|} \quad (2.6)$$

which amounts to a z -noise of 0.2 pm in the present example. Thus, in STM the noise in the tunneling current is not a problem, because it is much smaller than the required resolution.

The spectacular spatial resolution and relative ease of obtaining atomic resolution by STM rests on three properties of the tunneling current:

- As a consequence of the strong distance dependence of the tunneling current, even with a relatively blunt tip the chance is high that a single atom protrudes far enough out of the tip such that it carries the main part of the tunneling current;
- Typical tunneling currents are in the nano-ampere range - measuring currents of this magnitude can be done with a very good signal to noise ratio even with a simple experimental setup;
- Because the tunneling current is a monotonic function of the tip-sample distance, it is easy to establish a feedback loop which controls the distance such that the current is constant.

It is shown in the next section, that neither of these conditions is met in the case of the AFM and therefore, substantial hurdles had to be overcome before atomic resolution by AFM became possible.

2.2 Atomic Force Microscope (AFM)

Early on in the development of STM it became evident, that the forces which act between the tip and sample lead to elastic deformations of tip and sample which can cause artifacts like “giant corrugations”[81, 110] or a modified dependence of $I_t(z)$. It was found that these forces could be put to good use in the Atomic Force Microscope (AFM), introduced in 1985 by Binnig, Quate and Gerber [21].

2.2.1 Imaging signal in AFM

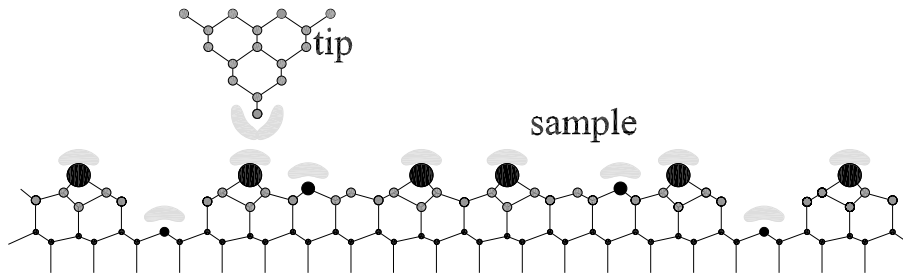


Figure 2.5: Schematic view of an AFM tip close to a sample.

Figure 2.5 shows a sharp tip close to a sample. The potential energy between the tip and sample V_{ts} causes a z component of the tip-sample force $F_{ts} = -\frac{\partial V_{ts}}{\partial z}$ and a “tip-sample spring constant” $k_{ts} = -\frac{\partial F_{ts}}{\partial z}$. Depending on the mode of operation, the AFM uses F_{ts} or some entity derived from F_{ts} as the imaging signal.

Unlike the tunneling current, which has a very strong distance dependence, F_{ts} has long- and short-range contributions. We can classify the contributions by their range and strength. In vacuum, there are van-der-Waals, electrostatic and magnetic forces with a long range (up to 100 nm) and short range chemical forces (fractions of nm). In ambient conditions, also meniscus forces formed by adhesion layers on tip and sample (water or hydrocarbons) can be present.

The van-der-Waals interaction is caused by fluctuations in the electric dipole moment of atoms and their mutual polarization. For two atoms at distance z , the energy varies as $1/z^6$ [15]. Assuming additivity and disregarding the discrete nature of matter by replacing the sum over individual atoms by an integration over a volume with

a continuous number density of atoms, the van-der-Waals interaction between macroscopic bodies can be calculated (“Hamaker approach”) [49]. This approach does not account for retardation effects due to the finite speed of light and is therefore only appropriate for distances up to several hundred Ångströms. For a spherical tip with radius R next to a flat surface (z is the distance between the plane connecting the centers of the surface atoms and the center of the closest tip atom) the van-der-Waals potential is given by [55]:

$$V_{LJ} = -\frac{A_H R}{6z}. \quad (2.7)$$

The “Hamaker constant” A_H depends on the type of materials (atomic polarizability and density) of the tip and sample. For most solids and interactions across vacuum, A_H is of the order of 1 eV. For a list of A_H for various materials, see [63]. The van-der-Waals interaction can be quite large – the typical radius of an etched metal tip is 100 nm and with $z = 0.5$ nm, the van-der-Waals energy is ≈ -30 eV, and the corresponding force is ≈ -10 nN.

A more modern approach to the calculation of van-der-Waals forces is described in [50], and other tip shapes are treated in [A4].

When the tip and sample are both conductive and have an electrostatic potential difference $U \neq 0$, electrostatic forces are important. For a spherical tip with radius R , the potential energy is given by [88]

$$V_{electrostatic}(z) = 2\pi\epsilon_0 R \sum_{n=2}^{\infty} \frac{\sinh(\alpha)}{\sinh(n\alpha)} U^2 \quad (2.8)$$

with

$$\alpha = \ln\left(1 + \frac{z}{R}\left(1 + \sqrt{1 + 2\frac{R}{z}}\right)\right). \quad (2.9)$$

Like the van-der-Waals interaction, the electrostatic interaction can also cause large forces – for a tip radius of 100 nm, $U = 1$ V and $z = 0.5$ nm, the electrostatic energy is ≈ -89 eV, and the corresponding force is ≈ -5.5 nN.

Electrostatic forces also arise in the imaging of ionic crystals, where the envelope of the electrostatic field has an exponential distance dependence [38].

Chemical forces are more difficult to describe. Empirical model potentials for chemical bonds are the Morse Potential (see e.g. [55]).

$$V_{Morse} = -E_{bond}(2e^{-\kappa(z-\sigma)} - e^{-2\kappa(z-\sigma)}) \quad (2.10)$$

and the Lennard-Jones potential [12, 55]:

$$V_{Lennard-Jones} = -E_{bond} \left(2 \frac{z^6}{\sigma^6} - \frac{z^{12}}{\sigma^{12}} \right). \quad (2.11)$$

These potentials describe a chemical bond with bonding energy E_{bond} and equilibrium distance σ . The Morse potential has an additional parameter – a decay length κ . While the Morse potential can be used for a qualitative description of chemical forces, it lacks an important property of chemical bonds: chemical bonds, especially covalent bonds show an inherent angular dependence of the bonding strength [26, 78]. Therefore, more sophisticated models like the Stillinger-Weber potential [94] are used in a more detailed description of the chemical interaction [A9].

More information about tip-sample forces can be found in Refs. [25, 55, 79, 80, 88, A4, A7] and references therein.

2.2.2 Experimental measurement and noise

Forces between the tip and sample are typically measured by recording the deflection of a cantilever beam that has a tip mounted to its end (see Fig. 2.6). While simple cantilevers can be cut from household tin foil [86], high-quality cantilevers are mainly built by micromachining silicon, where pioneering work was done in the group of Calvin F. Quate [2, 3, 100] and at IBM [111].

The cantilever bends in response to the forces between tip and sample. The cantilever is characterized by its spring constant k , eigenfrequency f_0 and quality factor Q . For

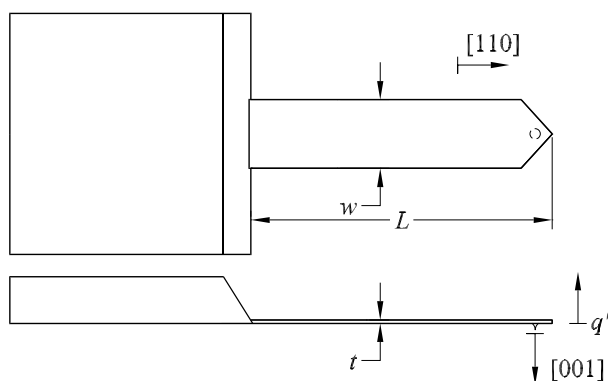


Figure 2.6: Top view and side view of a microfabricated silicon cantilever (schematic).

a rectangular cantilever with dimensions w , t and L (see Fig. 2.6), the spring constant k is given by [24]:

$$k = \frac{E_Y w t^3}{4L^3}. \quad (2.12)$$

where E_Y is Young's modulus. The eigenfrequency f_0 is given by [24]:

$$f_0 = 0.162 \frac{t}{L^2} \sqrt{\frac{E_Y}{\rho}} \quad (2.13)$$

where ρ is the mass density of the cantilever material. The Q -factor depends on the damping mechanisms present in the cantilever. For micromachined cantilevers operated in air, Q is typically a few hundred while in vacuum, Q can reach hundreds of thousands.

In the first AFM, the deflection of the cantilever was measured with an STM - the backside of the cantilever was metalized, and a tunneling tip was brought close to it to measure the deflection [21]. While the tunneling effect is very sensitive to distance variations, this method has a number of drawbacks. The tunneling tip also exerts forces on the cantilever, and it is quite difficult to position a tunneling tip close to a cantilever. Subsequent designs used optical (interferometer, beam-bounce) or electrical methods (piezoresistive, piezoelectric) for measuring the cantilever deflection. A discussion of the various techniques can be found in [88], and the appendix contains descriptions of piezoresistive [A1, A3] and piezoelectric [A5, A8] methods.

The deflection of the cantilever is subject to thermal drift and other noise factors. This can be expressed in a plot of the deflection noise density versus frequency. A typical noise density is plotted in Fig. 2.7. The noise density has a $1/f$ dependence for low frequency and merges into a constant noise density ("white noise") above the " $1/f$ corner frequency". This $1/f$ noise is also apparent in other force sensing devices, such as scales. Typically, scales have a reset or zero button, which allows the user to reset the effects of long-term drift. Machining AFMs from materials with low thermal expansion coefficients like Invar or operation at low temperatures helps to minimize $1/f$ noise.

In the dynamic operating modes (see next section), drifts in f_0 also add to the vertical noise. This is discussed in detail on page 45.

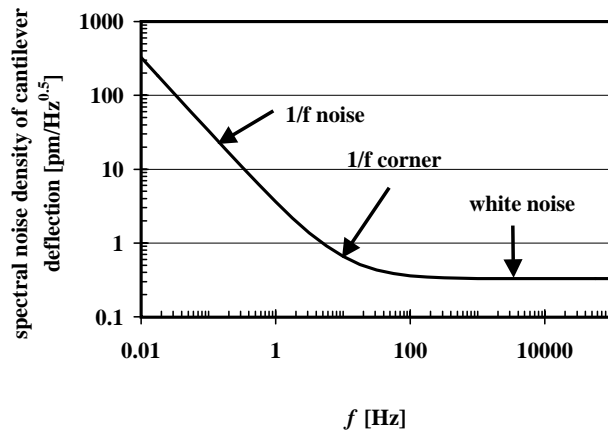


Figure 2.7: Schematic view of $1/f$ noise apparent in force detectors.

2.3 Operating Modes of AFMs

2.3.1 Static AFM

In the case of the AFM, the force F_{ts} which acts between the tip and sample is used as the imaging signal. In the static mode of operation, the force translates into a deflection $q' = F_{ts}/k$ of the cantilever. Because the deflection of the cantilever should be significantly larger than the deformation of the tip and sample, restrictions on the useful range of k apply. In the static mode, the cantilever should be much softer than the bonds between the bulk atoms in tip and sample. Interatomic force constants in solids are in a range from 10 N/m to about 100 N/m - in biological samples, they can be as small as 0.1 N/m. Thus, typical values for k in the static mode are 0.01 – 5 N/m.

The eigenfrequency f_0 should be significantly higher than the desired detection bandwidth, i.e. if 10 lines per second are recorded during imaging a width of say 100 atoms, f_0 should be at least $10 \times 2 \times 100 \text{ s}^{-1} = 2 \text{ kHz}$ in order to prevent resonant excitation of the cantilever.

Even though it has been demonstrated that atomic resolution is possible with static AFM, the method can only be applied in certain cases. The detrimental effects of $1/f$ -noise can be limited by working at low temperatures [38], where the coefficients of thermal expansion are very small or by building the AFM of a material with a

low thermal expansion coefficient [74]. The long-range attractive forces have to be cancelled by immersing tip and sample in a liquid [74] or by partly compensating the attractive force by pulling at the cantilever after jump-to-contact has occurred [37, 38, 39]. Jarvis *et al.* have cancelled the long-range attractive force with an electromagnetic force applied to the cantilever [57, 58]. Even with these restrictions, static AFM does not produce atomic resolution on reactive surfaces like silicon, as the chemical bonding of AFM tip and sample pose an unsurmountable problem [53]. While the experimental implication of static AFM is difficult, the physical interpretation of static AFM images is simple: The image is a map $z(x, y, F_{ts} = const.)$.

2.3.2 Dynamic AFM

In the dynamic operation modes, the cantilever is deliberately vibrated. The cantilever is mounted onto an actuator to allow an external excitation of an oscillation. There are two basic methods of dynamic operation: amplitude modulation (AM) - and frequency modulation (FM) operation. In AM-AFM [71], the actuator is driven by a fixed amplitude A_{drive} at a fixed frequency f_{drive} where f_{exc} is close to but different from f_0 . When the tip approaches the sample, elastic and inelastic interactions cause a change in both the amplitude and the phase (relative to the driving signal) of the cantilever. These changes are used as the feedback signal. The change in amplitude in AM mode does not occur instantaneously with a change in the tip-sample interaction, but on a timescale of $\tau_{AM} \approx 2Q/f_0$. With Q -factors reaching 100000 in vacuum, this means that the AM mode is very slow. Albrecht and coworkers found a way around this problem by introducing the frequency modulation (FM) mode [4], where the change in the eigenfrequency settles on a timescale of $\tau_{FM} \approx 1/f_0$.

Both AM and FM modes were initially meant to be “non-contact” modes, i.e. the cantilever was far away from the surface and the net force between the front atom of the tip and the sample was clearly attractive. The AM mode was later used very successfully at a closer distance range in ambient conditions involving repulsive tip-sample interactions (“Tapping Mode” [112]) and Erlandsson *et al.* obtained atomic resolution on Si in vacuum with an etched tungsten cantilever operated in AM mode in 1996 [34]. Using the FM mode, the resolution was improved dramatically [A1, 40]

and finally atomic resolution [A2] was obtained by reducing the tip sample distance and working in vacuum. While it was believed initially that the net force between the front atom of the tip and the sample has to be attractive when atomic resolution is desired, this view has been challenged recently [93]. Nevertheless, the dynamic modes are commonly still called “non-contact” modes and the conference series which covers AFM with atomic resolution in vacuum is named “International Conference on Non-contact Atomic Force Microscopy”. It is noted, that the definition of “contact” between two objects (tip and sample) is difficult when looking on atomic length scales – even though on a macroscopic scale the definition of “contact” between two objects is perfectly clear. What is commonly understood by “Non-contact AFM” is that neither tip nor sample suffer permanent deformations or wear during the imaging process – no matter whether the force between tip and sample or the force between the front atom of the tip and the sample is attractive or repulsive. For atomic studies in vacuum, the FM-mode is now the preferred AFM technique. A detailed description of the FM-mode is given in chapter 4.

Chapter 3

The four additional challenges faced by AFM

In a scanning tunneling microscope, a tip has to be scanned across a surface with a precision of fractions of an Ångström while a feedback mechanism adjusts the z -position such that the tunneling current is constant. This task seems daunting and the successful realization of STM is an amazing accomplishment. Yet, implementing an AFM capable of atomic resolution poses even more obstacles than the operation of an STM. Some of the additional challenges faced by AFM are apparent by comparing the tunneling current and tip sample force as a function of distance (Fig. 3.1). The

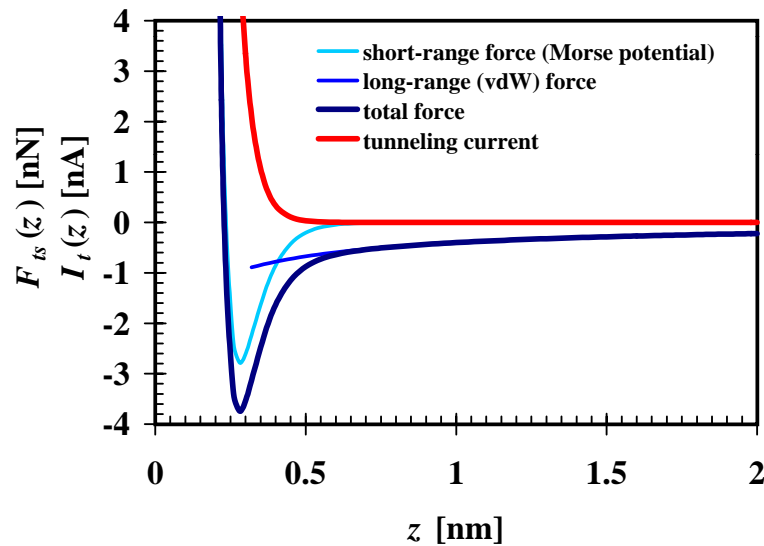


Figure 3.1: Plot of tunneling current I_t and force F_{ts} (typical values) as a function of distance z between front atom and surface atom layer.

tunneling current is a monotonic function of the tip-sample distance and has a very sharp distance dependence. In contrast, the tip-sample force has long- and short-range components and is not monotonic.

3.1 Jump-to-contact problem

Van-der-Waals forces in vacuum are always attractive, and if chemical bonding between tip and sample can occur the chemical forces are also attractive for distances larger than the equilibrium distance. Because the tip is mounted on a spring, approaching the tip can cause a sudden “jump to contact” when the stiffness of the cantilever is smaller than a certain value.

This instability occurs in the quasistatic mode if [98, 23]

$$k > \max\left(-\frac{\partial^2 V_{ts}}{\partial z^2}\right) = k_{ts}^{\max}. \quad (3.1)$$

The jump to contact can be avoided even for soft cantilevers by oscillating it at a large enough amplitude A [A3]:

$$kA > \max(-F_{ts}) = F_{ts}^{\max}. \quad (3.2)$$

It has been found empirically (see column 5 in table 4.1), that $kA \approx 200$ nN for avoiding this instability. With typical spring constants of $k \approx 20$ N/m, amplitudes in the range of $A \approx 10$ nm are required. However, using large amplitudes has critical disadvantages, which are discussed in chapter 6.

3.2 Non-monotonic imaging signal

The magnitude of the tunneling current increases continuously as the tip-sample distance decreases, i.e. the tunneling current is a strictly monotonic decreasing function of the distance (see Fig. 2.4 on page 11). This property allows a simple implementation of a feedback loop: the tunneling current is fed into a logarithmic amplifier to produce an error signal that is linear with the tip-sample distance.

In contrast, the tip-sample force is not monotonic. In general, the force is attractive for large distances and upon decreasing the distance between tip and sample, the

force turns repulsive (see Fig. 3.1). Stable feedback is only possible on a branch of the force curve, where it is monotonic.

Because the tunneling current is monotonic for the whole distance range and the tip-sample force is not monotonic, it is much easier to establish a z - distance feedback loop for STMs than for AFMs.

3.3 Contribution of long-range forces

The force between tip and sample is composed of many contributions: electrostatic, magnetic, van-der-Waals and chemical forces in vacuum. In ambient conditions there are also meniscus forces. While electrostatic-, magnetic- and meniscus forces can be eliminated by working in vacuum with nonmagnetic tips and equalizing the electrostatic potential between tip and sample, the van-der-Waals forces cannot be switched off. For imaging by AFM with atomic resolution, it is desirable to filter out the long-range force contributions and only measure the force components which vary at the atomic scale. In STM, the strong distance dependence of the tunneling current naturally enables high resolution. While there is no way to discriminate between long- and short-range forces in static AFM, it is shown in section 5.2 that it is possible to enhance the short-range contributions in dynamic AFM by proper choice of the oscillation amplitude A of the cantilever.

3.4 Noise in the imaging signal

Forces can be measured by the deflection of a spring. However, measuring the deflection is not a trivial task and is subject to noise, especially at low frequencies ($1/f$ noise). In static AFM, the imaging signal is given by the dc deflection of the cantilever, which is subject to $1/f$ noise. In dynamic AFM, the low-frequency noise is discriminated if the eigenfrequency f_0 is larger than the $1/f$ corner frequency. With a bandpass filter with a center frequency around f_0 only the white noise density is integrated across the bandwidth B of the bandpass filter.

Frequency modulation AFM, described in detail in chapter 4, helps to overcome three

of these four challenges. The non-monotonic imaging signal in AFM is a remaining complication for FM-AFM.

Chapter 4

Frequency-modulation AFM (FM-AFM)

4.1 Experimental setup

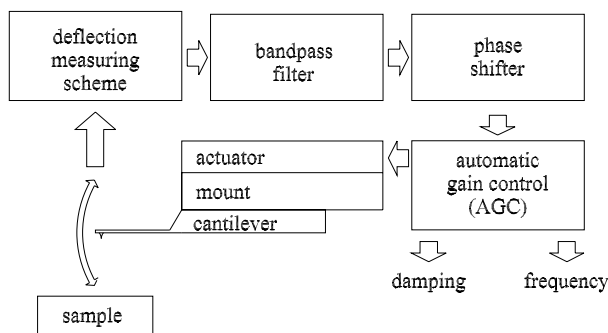


Figure 4.1: Block diagram of a frequency-modulation force sensor.

In FM-AFM, a cantilever with eigenfrequency f_0 and spring constant k is subject to controlled positive feedback such that it oscillates with a constant amplitude A [4] as shown in Fig. 4.1. The deflection signal is phase shifted, routed through an automatic gain control circuit and fed back to the actuator. The frequency f is determined by the eigenfrequency f_0 of the cantilever and the phase shift φ between the mechanical excitation generated at the actuator and the deflection of the cantilever. If $\varphi = \pi/2$, the loop oscillates at $f = f_0$.

Forces between tip and sample cause a change in $f = f_0 + \Delta f$. If the second derivative of the tip-sample potential $k_{ts} = \frac{\partial^2 V_{ts}}{\partial z^2}$ is constant for the whole range covered by the

oscillating cantilever, the shift in eigenfrequency that occurs is given by:

$$\Delta f = \frac{k_{ts}}{2k} f_0. \quad (4.1)$$

The case where k_{ts} is not constant is treated in the next chapter. By measuring the frequency shift Δf , the tip-sample forces can be determined.

The oscillator circuit is a critical component in FM-AFM and has been home-built for our experiments. The function of this device is understood best by analyzing the cantilever motion. The cantilever can be treated as a damped harmonic oscillator that is externally driven. For sinusoidal excitations $A_{drive} e^{i2\pi f_{drive} t}$ and a quality factor $Q \gg 1$, the response of the oscillation amplitude of the cantilever is given by

$$\frac{A}{A_{drive}} = \frac{1}{1 - f_{drive}^2/f_0^2 + i f_{drive}/(f_0 Q)}. \quad (4.2)$$

The absolute value of the amplitude is given by

$$|A| = \frac{|A_{drive}|}{\sqrt{(1 - f_{drive}^2/f_0^2)^2 + f_{drive}^2/(f_0^2 Q^2)}} \quad (4.3)$$

and the phase angle between the driving and resulting signals is

$$\varphi = \arctan\left[\frac{f_{drive}}{Q f_0 (1 - f_{drive}^2/f_0^2)}\right] \quad (4.4)$$

In the case of a closed feedback loop as shown in Fig. 4.1, the driving frequency cannot be chosen freely anymore but is determined by f_0 of the cantilever, the phase shift φ and the tip-sample forces. The purpose of the oscillator circuit is to provide controlled positive feedback (with a phase angle of $\varphi = \pi/2$) such that the cantilever oscillates at a constant amplitude. This requirement is fulfilled with the setup shown in Fig. 4.2.

The cantilever deflection signal enters to the left and is first routed through a band-pass filter which cuts off the noise from unwanted frequency bands. While this filter is not absolutely necessary (a cantilever with a high Q -value is already an excellent mechanical bandpass), it helps for observing the deflection signal on an oscilloscope. The filtered deflection signal branches into an rms-to-dc converter and a phase shifter (see [52]). The rms-to-dc chip (e.g. AD 536A [9]) computes a dc signal which corresponds to the rms-value of the amplitude. This signal is added to the inverted

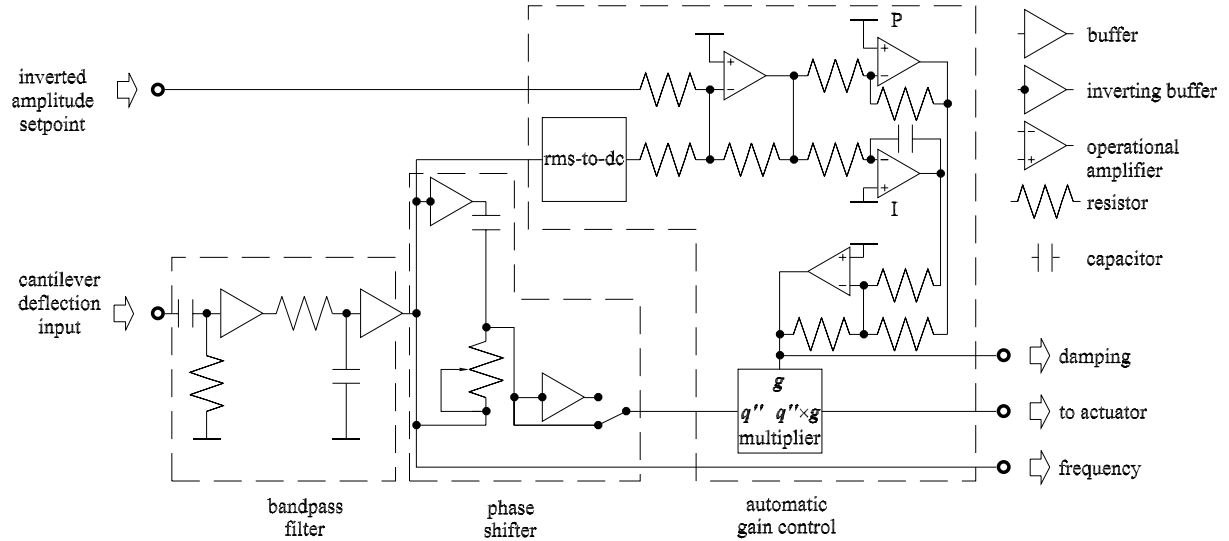


Figure 4.2: Block diagram of the oscillator control electronics for frequency-modulation detection.

setpoint rms amplitude, yielding the amplitude error signal. The amplitude error enters a proportional (P) and optional integral (I) controller and the resulting signal g is multiplied with the phase shifted cantilever deflection signal q'' with an analog multiplier chip (e.g. AD 534 [9]). This signal drives the actuator. The phase shifter is adjusted so that the driving signal required for establishing the desired oscillation amplitude is minimal; φ is exactly $\pi/2$ in this case.

The filtered cantilever deflection signal is fed into a commercial phase-locked-loop (PLL) detector [73]. The PLL allows to set a reference frequency f_{ref} and outputs a signal which is proportional to the difference between the input frequency f and the reference frequency f_{ref} . This signal $\Delta f = f - f_{ref}$ is used as the imaging signal in FM-AFM.

Conservative tip-sample forces cause a frequency shift. A non-conservative component in the tip-sample force, that is a hysteresis in the force versus distance graph

$$\Delta E_{ts} = \int_{-A}^A F_{ts}(z + z') dz' + \int_A^{-A} F_{ts}(z + z') dz', \quad (4.5)$$

causes extra dissipation in the motion of the cantilever. When the tip of the cantilever is far from the sample, the damping of the cantilever is due to internal dissipation

and the energy loss per oscillation cycle is given by:

$$\Delta E_{CL} = 2\pi \frac{E}{Q} \quad (4.6)$$

where $E = kA^2/2$ is the energy of the cantilever and Q is its quality factor. When the phase angle between the excursion of the actuator and the excursion of the cantilever is exactly $\varphi = \pi/2$, the cantilever oscillates at frequency f_0 and the driving signal is $A_{drive} = Ae^{i\pi/2}/Q$. Hence, the driving amplitude and dissipation are connected:

$$|A_{drive}| = |A| \frac{\Delta E_{CL}}{2\pi E}. \quad (4.7)$$

When the tip oscillates close to the sample, additional damping occurs and the driving signal A_{drive} is increased by the oscillator control electronics to A'_{drive} for maintaining a constant amplitude A where

$$|A'_{drive}| = |A| \frac{\Delta E_{CL} + \Delta E_{ts}}{2\pi E} = |A| \left(\frac{1}{Q} + \frac{\Delta E_{ts}}{2\pi E} \right). \quad (4.8)$$

Equation 4.8 has an important implication on the optimal Q factor of the cantilever. While a high Q factor results in low frequency noise (see Eq. 6.6 on page 44), Eq. 4.8 shows that the Q value of the cantilever should not be much higher than the ratio $2\pi E/\Delta E_{ts}$. If Q is much higher than this value, it is difficult for the oscillator circuit to maintain a constant amplitude, because small changes in ΔE_{ts} require a major correction in the control output g .

Measuring the damping signal yields the dissipation in the approach and retract phases of the oscillating tip where

$$\Delta E_{ts} = 2\pi \frac{E}{Q} \left(\frac{|A'_{drive}|}{|A_{drive}|} - 1 \right). \quad (4.9)$$

The ratio $|A'_{drive}|/|A_{drive}|$ is easily accessible in the dc input (g) of the analog multiplier chip in Fig. 4.2 – an increase in the tip-sample dissipation ΔE_{ts} is reflected in an increased gain signal g' in the oscillator electronics and $g'/g = |A'_{drive}|/|A_{drive}|$. Several authors have recorded this signal simultaneously with the frequency shift and thus measured both elastic and non-elastic interaction forces simultaneously, see e.g. [13, 103].

It is noted, that dispersions in the oscillator circuit and in the actuator assembly can lead to artifacts in the interpretation of damping data, because $|A_{drive}| = |A|/Q$

only holds for $f = f_0$. Anczykowski *et al.* [10] have introduced a method that yields the correct dissipation energy even for cases where the phase angle between actuator and cantilever is not $\varphi = \pi/2$. Mechanical resonances in the actuator assembly are likely to occur at the high resonance frequencies of conventional cantilevers. These resonances can cause sharp variations of the phase with frequency and thus create artifacts in the measurement of ΔE_{ts} . A self-oscillation technique for cantilevers [A3] helps to avoid these resonances.

4.2 Applications

FM-AFM was introduced by Albrecht and coworkers in magnetic force microscopy [4]. In these experiments, Albrecht *et al.* imaged a thin film CoPtCr magnetic recording disk (Fig. 7a in [4]) with a cantilever with a spring constant $k \approx 10$ N/m, eigenfrequency $f_0 = 68.485$ kHz, amplitude $A = 5$ nm, a Q value of 40000 [5] and a tip with a thin magnetic film coverage. The noise level and imaging speed was enhanced significantly compared to amplitude modulation techniques. In 1993, the frequency modulation method was implemented in the prototype of a commercial STM/AFM for ultra-high vacuum [A1]. Initial experiments on KCl yielded excellent resolution and soon after, the Si (111)-(7×7) surface was imaged with true atomic resolution for the first time [A2].

FM-AFM has four operating parameters:

1. The spring constant of the cantilever k .
2. The eigenfrequency of the cantilever f_0 .
3. The oscillation amplitude A .
4. The frequency shift of the cantilever Δf .

The first two parameters are determined by the type of cantilever that is used, while the latter two parameters can be freely adjusted. The initial parameters which provided true atomic resolution ($k = 17$ N/m, $f_0 = 114$ kHz, $A = 34$ nm, $\Delta f = -70$ Hz) were found empirically. Surprisingly, the amplitude necessary for obtaining good results was very large compared to atomic dimensions. The necessity of using large

amplitudes for obtaining good results seems counterintuitive, because the tip of the cantilever spends only a small fraction during an oscillation cycle in close vicinity to the sample. In hindsight, it is clear that the large amplitudes were required to prevent jump-to-contact (see section 3.1). Obviously, the product between spring constant and amplitude (column “ kA [nN]” in Table 4.1) has to be larger than ≈ 100 nN to provide a sufficiently strong withdrawing force. In the experiments conducted in 1994 (see rows 1 and 2 in Table 4.1), this condition was not met, and correspondingly, the resolution was not quite atomic yet. It is also speculated, that $E = \frac{1}{2}kA^2$ (column “ E [keV]” in Table 4.1) should be large compared to ΔE_{ts} defined in Eq. 4.1. As shown in Table 4.1, atomic resolution on silicon and other samples was reproduced by other groups with similar operating parameters $\Delta f \approx -100$ Hz, $k \approx 20$ N/m, $f_0 \approx 200$ kHz and $A \approx 10$ nm. Several commercial vendors now offer FM-AFMs that operate with these parameters [59, 75, 99]. Because many FM-AFMs operating with this initial parameter set are in use, we call this operating mode the “classic” FM-AFM mode.

While the operating parameters of the classic FM-AFM mode provide good results routinely, it was not proven initially that these parameters yield optimal resolution. The search space for finding the optimal parameters was not completely open, because micromachined cantilevers were only available with a limited selection of spring constants. A theoretical study has shown later [A6], that the optimal spring constants should be of the order of a few hundred N/m, much stiffer than the spring constant of commercially available cantilevers. This result has been verified experimentally recently by achieving unprecedented resolution with a cantilever with $k = 1800$ N/m [A9].

year	k [N/m]	f_0 [kHz]	Δf [Hz]	A [nm]	kA [nN]	E [keV]	sample	Ref.:
1994	2.5	60.0	-16	15.0	37.5	1.8	KCl(001)*	[A1]
1994	2.5	60.0	-32	3.3	8.25	0.1	Si(111)*	[40]
1995	17.0	114.0	-70	34.0	544	61	Si(111)	[A2]
1995	43.0	276.0	-60	40.0	1720	215	Si(111)	[61]
1995	34.0	151.0	-6	20.0	680	42	InP(110)	[96]
1996	23.5	153.0	-70	19.0	447	27	Si(111)	[69]
1996	33.0	264.0	-670	4.0	132	12	Si(001)	[62]
1996	10.0	290.0	-95	10.0	100	3.1	Si(111)	[48]
1997	30.0	168.0	-80	13.0	390	16	NaCl(001)	[13]
1997	28.0	270.0	-80	15.0	420	20	TiO ₂ (110)	[35]
1997	41.0	172.0	-10	16.0	654	33	Si(111)	[97]
1999	35.0	160.0	-63	8.8	338	10	HOPG(0001)	[7]
1999	36.0	160.0	-60.5	12.7	457	18	InAs(110)	[92]
1999	36.0	160.0	-92	9.4	338	10	Xe(111)	[8]
2000	28.6	155.7	-31	5	143	2.2	Si(111)	[66]
2000	1800	16.86	-160	0.8	1440	3.6	Si(111)	[A9]
2000	1800	20.53	85	0.3	540	0.5	Si(111)	[A10]

Table 4.1: Cantilever properties (k , f_0) and operating parameters (Δf , A , E) of various FM-AFM experiments.

*Atomic resolution was not achieved in these initial experiments.

Chapter 5

Calculation of the frequency shift in FM-AFM

5.1 Generic calculation

The oscillation frequency is the observable in FM-AFM and it is important to establish a connection between frequency shift and the forces acting between tip and sample. While the frequency can be calculated numerically [11], an analytic calculation is important for finding the functional relationships between operational parameters and the physical tip-sample forces. The motion of the cantilever (spring

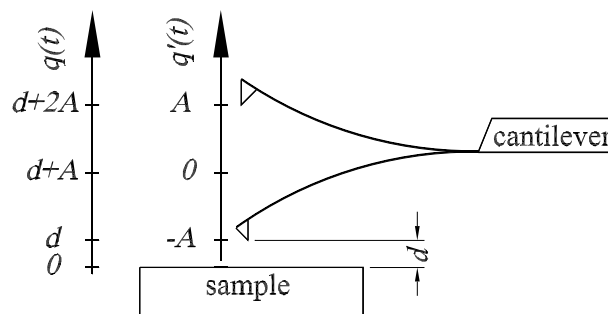


Figure 5.1: Schematic view of an oscillating cantilever and definition of geometric terms.

constant k , effective mass m^*) can be described by a weakly disturbed harmonic oscillator. Figure 1 shows the deflection $q'(t)$ of the tip of the cantilever: it oscillates with an amplitude A at a distance $q(t)$ to a sample. The closest point to the sample

is $q = d$ and $q(t) = q'(t) + d + A$. The Hamiltonian of the cantilever is:

$$H = \frac{p^2}{2m^*} + \frac{kq'^2}{2} + V_{ts}(q) \quad (5.1)$$

where $p = m^*dq'/dt$. The unperturbed motion is given by:

$$q'(t) = A \cos(2\pi f_0 t) \quad (5.2)$$

and the frequency is:

$$f_0 = \frac{1}{2\pi} \sqrt{\frac{k}{m^*}}. \quad (5.3)$$

If the force gradient $k_{ts} = -\frac{\partial F_{ts}}{\partial z}$ is constant during the oscillation cycle, the calculation of the frequency shift is trivial:

$$\Delta f = f_0 \frac{k_{ts}}{2k}. \quad (5.4)$$

However, in classic FM-AFM k_{ts} varies orders of magnitude during one oscillation cycle and a perturbation approach as shown below has to be employed for the calculation of the frequency shift.

5.1.1 Hamilton-Jacobi Method

The first derivation of the frequency shift in FM-AFM was achieved in 1997 [A3] using canonical perturbation theory [43]. The result of this calculation is:

$$\Delta f = -\frac{f_0}{kA^2} \langle F_{ts}q' \rangle. \quad (5.5)$$

where the pointed brackets indicate averaging across one oscillation cycle.

The applicability of first-order perturbation theory depends on the magnitude of the perturbation, i.e. on the ratio between V_{ts} and the energy of the oscillating cantilever $E = H_0$. In FM-AFM, E is typically in the range of several keVs (see table 4.1), while V_{ts} is only a few electron volts and first order perturbation theory yields results for Δf with excellent precision.

5.1.2 Fourier Method

An alternate approach to the calculation of Δf has been shown by Baratoff [14], Dürig [29] and Livshits *et al.* [67]. This approach also derives the magnitude of the higher harmonics and the constant deflection of the cantilever.

This method involves solving Newton's equation of motion for the cantilever (effective mass μ^* , spring constant k):

$$\mu^* \frac{d^2 q'}{dt^2} = -kq' + F_{ts}(q'). \quad (5.6)$$

Using a Fourier series with fundamental frequency f :

$$q'(t) = \sum_{m=0}^{\infty} a_m \cos(m2\pi ft). \quad (5.7)$$

Insertion into Eq. 5.6 yields:

$$\sum_{m=0}^{\infty} a_m \left[-(m2\pi f)^2 \mu^* + k \right] \cos(m2\pi ft) = F_{ts}(q'). \quad (5.8)$$

Multiplication by $\cos(l2\pi ft)$ and integration from $t = 0$ to $t = 1/f$ yields:

$$a_m \left[-(m2\pi f)^2 \mu^* + k \right] \pi(1 + \delta_{m0}) = 2\pi f \int_0^{1/f} F_{ts}(q') \cos(m2\pi ft) dt \quad (5.9)$$

by making use of the orthogonality of the angular functions

$$\int_0^{2\pi} \cos(mx) \cos(lx) dx = \pi \delta_{ml} (1 + \delta_{m0}). \quad (5.10)$$

If the perturbation is weak, $q'(t) \approx A \cos(2\pi ft)$ with $f = f_0 + \Delta f$, $f_0 = \frac{1}{2\pi} \sqrt{\frac{k}{\mu^*}}$ and $|\Delta f| \ll f_0$. To first order, the frequency shift is given by:

$$\Delta f = -\frac{f_0^2}{kA} \int_0^{1/f_0} F_{ts}(q') \cos(2\pi f_0 t) dt = -\frac{f_0}{kA^2} \langle F_{ts} q' \rangle. \quad (5.11)$$

Thus, the Fourier approach yields the same result for Δf as the Hamilton-Jacobi method.

In addition, the amplitudes of the higher harmonics:

$$a_m = \frac{2f_0}{k(1 + \delta_{m0})(1 - m^2)} \int_0^{1/f_0} F_{ts}(q') \cos(m2\pi f_0 t) dt \quad (5.12)$$

and the mean displacement of the cantilever:

$$a_0 = \frac{f_0}{k} \int_0^{1/f_0} F_{ts}(q') dt = \frac{1}{k} \langle F_{ts} \rangle \quad (5.13)$$

are found by this approach. Dürig [30] has estimated the magnitude of the higher harmonics by using:

$$\left| \int_0^{1/f_0} F_{ts}(q') \cos(m2\pi f_0 t) dt \right| < \left| \int_0^{1/f_0} F_{ts}(q') \cos(2\pi f_0 t) dt \right|. \quad (5.14)$$

Thus for $m > 1$:

$$|a_m| \leq A \frac{2}{m^2 - 1} \left| \frac{\Delta f}{f_0} \right|. \quad (5.15)$$

For typical experiments $\Delta f/f_0 < 10^{-3}$, i.e. the higher harmonics are small compared to the fundamental amplitude A .

The results of these calculations are also applicable for amplitude modulation AFM [17].

Hölscher *et al.* [51] have used canonical perturbation theory to derive the first analytic results for the frequency shift caused by inverse power forces. Sasaki and Tsukada have obtained a similar result to Eq. 5.5 with a different type of perturbation theory [89, 90].

Dürig has shown, that in principal the tip sample potential can be reconstructed when the amplitudes and phases of the higher harmonics are known [31].

5.1.3 A very simple expression for frequency shifts as a function of the tip-sample forces

For small amplitudes, the frequency shift is a very simple function of the tip-sample forces – it is proportional to the tip-sample force gradient k_{ts} . For large amplitudes, the frequency shift is given by the rather complicated expressions Eq. 5.5 and Eq. 5.11. With integration by parts, these complicated formulas transform into a very simple expression that resembles Eq. 5.4 [A11].

$$\Delta f(z) = f_0 \frac{\langle k_{ts}(z) \rangle}{2k} \quad (5.16)$$

with

$$\langle k_{ts}(z) \rangle = \frac{1}{\frac{\pi A^2}{2}} \int_{-A}^A k_{ts}(z - q') \sqrt{A^2 - q'^2} dq'. \quad (5.17)$$

This expression is closely related to Eq. 5.4: the constant k_{ts} of Eq. 5.4 is replaced by a weighted average $\langle k_{ts} \rangle$, where the weight function $w(q', A)$ is a semi circle with radius A divided by the area of the semicircle $\Gamma = \pi A^2/2$ (see Fig. 2 (b) in Ref. [A11]).

5.2 Frequency shift for a typical tip-sample force

The interaction of a macroscopic tip of an AFM with a sample is a complicated many-body problem and F_{ts} cannot be described by a simple function. However, quite realistic model forces can be constructed from linear combinations of the following basic types: a) inverse-power forces, b) power forces and c) exponential forces. Analytic expressions for the frequency shift as a function of z and A are listed in Ref. [A7]. A typical tip-sample force is composed of long range contributions and short range contributions [A4]. This force can be approximated by a long-range van-der-Waals component and a short-range Morse type interaction:

$$F_{ts}(z) = \frac{C}{z + \sigma} + 2\kappa E_{bond} (-e^{-\kappa(z-\sigma)} + e^{-2\kappa(z-\sigma)}). \quad (5.18)$$

C depends on the tip angle and the Hamaker constant of tip and sample [A4], and E_{bond} , σ and κ are the bonding energy, equilibrium distance and decay length of the Morse potential respectively. With the results derived in [A7], the resulting frequency shift is:

$$\begin{aligned} \Delta f(z, A) = & \frac{f_0}{kA} \frac{C}{z + \sigma} \left[F_1^{1,1/2} \left(\frac{-2A}{z + \sigma} \right) - F_2^{1,3/2} \left(\frac{-2A}{z + \sigma} \right) \right] \\ & - f_0 \frac{2\kappa E_{bond}}{kA} \left\{ e^{-\kappa z} \left[M_1^{1/2}(-2\kappa A) - M_2^{3/2}(-2\kappa A) \right] \right. \\ & \left. + e^{-2\kappa z} \left[M_1^{1/2}(-4\kappa A) - M_2^{3/2}(-4\kappa A) \right] \right\}. \end{aligned} \quad (5.19)$$

where $F_c^{a,b}(z)$ is the Hypergeometric Function and $M_b^a(z)$ is Kummer's Function [1].

Equation 5.19 describes the frequency shift as a function of amplitude. For small amplitudes, the frequency shift is independent of the amplitude and proportional to

the tip-sample force gradient k_{ts} (Eq. 5.4). For amplitudes that are large compared to the range of the tip-sample force, the frequency shift is described by a “normalized frequency shift” γ given by:

$$\gamma(z, A) := \frac{kA^{3/2}}{f_0} \Delta f(z, A) \quad (5.20)$$

where $\gamma(z, A)$ asymptotically approaches a constant value for sufficiently large amplitudes (see Fig. 2 in Ref. [A7]), i.e. $\lim_{A \rightarrow \infty} \gamma(z, A) \equiv \gamma_{lA}(z)$. This normalized frequency shift is calculated from the tip-sample force according to [A7]:

$$\gamma_{lA}(z) = \frac{1}{\sqrt{2\pi}} \int_0^\infty \frac{F_{ts}(z+z')}{\sqrt{z'}} dz'. \quad (5.21)$$

Thus, for small amplitudes the frequency shift is very sensitive to short-range forces, because short-range forces have a very strong force gradient, while for large amplitudes, long-range forces contribute heavily to the frequency shift. Figure 5.2 shows the tip-sample force defined in Eq. 5.18 and the corresponding force gradient and normalized frequency shift γ_{lA} . The parameters for the short-range interaction are adopted from Perez *et al.* [80]: $\kappa = 12.76 \text{ nm}^{-1}$, $E_{bond} = 2.273 \text{ eV}$ and $\sigma = 2.357 \text{ \AA}$. The force gradient is vanishing for $z > 6 \text{ \AA}$, while the normalized frequency shift for

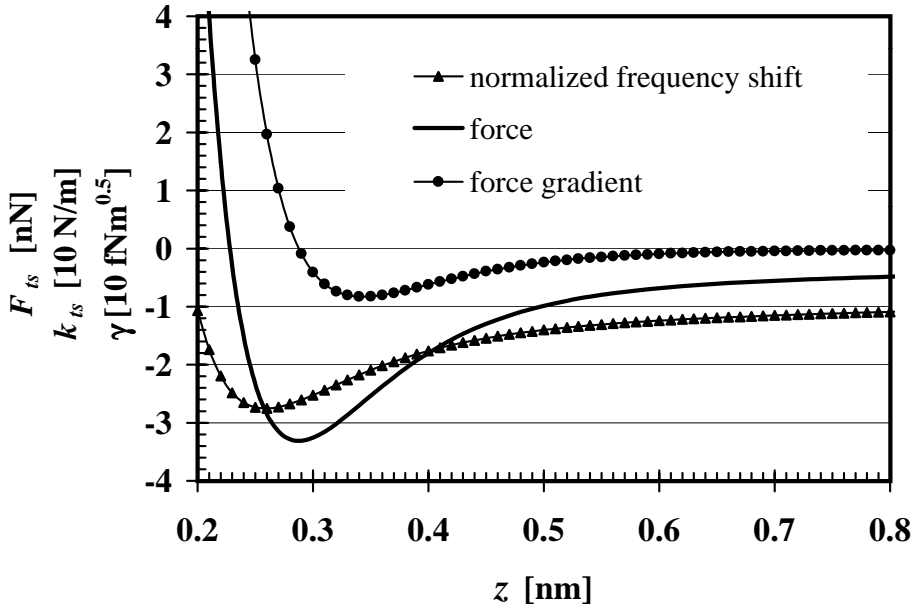


Figure 5.2: Force $F_{ts}(z)$, force gradient $k_{ts}(z)$ and normalized frequency shift $\gamma(z)$ for the tip-sample force defined in Eq. 5.18.

large amplitudes reaches almost half its maximum at this distance. The dependence of the frequency shift with amplitude leads to an important conclusion: small amplitudes increase the sensitivity to short-range forces! The possibility of adjusting the amplitude in FM-AFM compares to tuning an optical spectrometer to a passing wavelength. When short-range interactions are to be probed, the amplitude should be in the range of the short-range forces. While using amplitudes in the Å-range has been elusive with conventional cantilevers because of the jump-to-contact problem described in section 3.1, the home-made force sensor described in chapter 7 is suited well for small-amplitude operation.

5.3 Calculation of the tunneling current for oscillating tips

When the tip of the cantilever and the sample are both conductive, simultaneous STM and FM-AFM operation is possible, i.e. the tunneling current I_t as well as the frequency shift can be recorded while scanning the surface. In most cases, the bandwidth of the tunneling current-preamplifier is much smaller than the oscillation frequency f_0 of typical cantilevers. The measured tunneling current is given by the time-average over one oscillation cycle. With the exponential distance dependence $I_t(z) = I_0 e^{-2\kappa_t z}$ (see Eq. 2.1) we find:

$$\langle I_t(z, A) \rangle = I_0 e^{-2\kappa_t z} M_1^{1/2}(-2\kappa_t A) \quad (5.22)$$

where $M_b^a(\zeta)$ is the Kummer Function [1]. When $\kappa_t A \gg 1$,

$$\langle I_t(z, A) \rangle \approx I_t(z, 0) / \sqrt{2\pi\kappa_t A}. \quad (5.23)$$

Figure 5.3 shows the dependence of the tunneling current as a function of the product between κ_t and A . For $A = 10$ nm and $\kappa_t = 1 \text{ \AA}^{-1}$, the mean tunneling current is $\approx 1/25$ of the value when the cantilever does not oscillate. Because the noise of the current measurement decreases with an increasing mean tunneling current, the use of small amplitudes improves simultaneous STM and FM-AFM measurements.

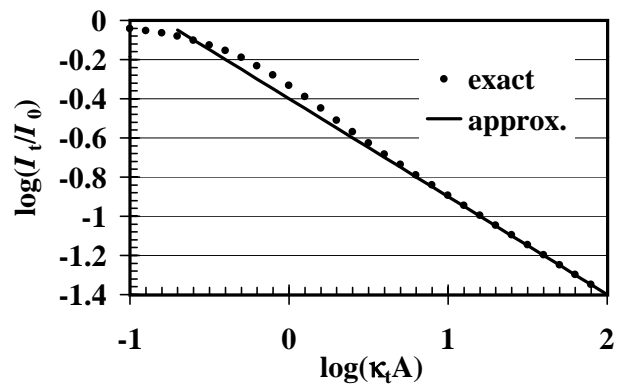


Figure 5.3: Plot of the mean tunneling current as a function of amplitude.

Chapter 6

Noise in frequency modulation AFM

6.1 Generic calculation

The vertical noise in FM-AFM can be calculated in the same fashion as in the STM case (see Fig. 2.4); it is given by the ratio between the noise in the imaging signal and the slope of the imaging signal with respect to z :

$$\delta z = \frac{\delta \Delta f}{\left| \frac{\partial \Delta f}{\partial z} \right|}. \quad (6.1)$$

Figure 6.1 shows a typical frequency shift versus distance curve. Because the distance between the tip and sample is measured indirectly through the frequency shift, it is clearly evident from Fig. 6.1 that the noise in the frequency measurement $\delta \Delta f$ translates into vertical noise δz and is given by the ratio between $\delta \Delta f$ and the slope of the frequency shift curve $\Delta f(z)$ (Eq. 6.1). Low vertical noise is obtained for a low-noise frequency measurement and a steep slope of the frequency shift curve.

Because the frequency shift is not monotonic with respect to z , stable feedback of the microscope is only possible either on the branch of Δf with positive slope or on the one with negative slope. In FM-AFM with atomic resolution, the branch with positive slope is usually chosen. However, when using very small amplitudes, it is also possible to work on the branch with negative slope (see Ref. [A10]).

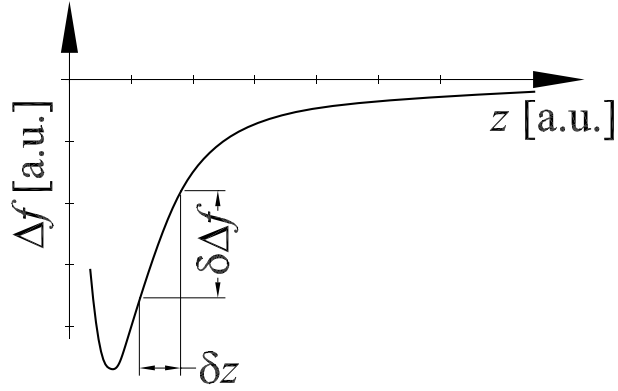


Figure 6.1: Plot of frequency shift Δf as a function of tip-sample distance z . The noise in the tip-sample distance measurement is given by the noise of the frequency measurement Δf divided by the slope of the frequency shift curve.

6.2 Noise in the frequency measurement

6.2.1 Fluctuations of the cantilever deflection

Equation 6.1 shows, that the accuracy of the frequency shift measurement determines directly the vertical resolution in FM-AFM. What is the accuracy of the measurement of the oscillation frequency of the cantilever? Martin *et al.* [71] and Albrecht *et al.* [4] have calculated the thermal limit of the frequency noise. Here, an empirical calculation of the frequency noise is introduced, because for most practical cases, the thermal limit is much lower than the actual instrumental deflection noise. The estimation introduced here obtains both the thermal limit of the frequency noise and the actual frequency noise when the deflection noise is larger than the thermal limit.

The frequency is given by the inverse of the time lag Ξ between two consecutive zero-crossings of the cantilever with positive velocity. However, the deflection of the cantilever q' is subject to a noise level $\delta q'$ as shown in Fig. 6.2. The deflection noise $\delta q'$ has two major contributions: a) thermal fluctuations of the cantilever and b) instrumental noise in the measurement of the deflection q' . The oscillation period Ξ can only be measured with an rms accuracy $\delta \Xi$. The uncertainty of the time of the zero-crossing is $\delta \Xi/2$, where $\delta \Xi/2$ is given by the ratio between the cantilever

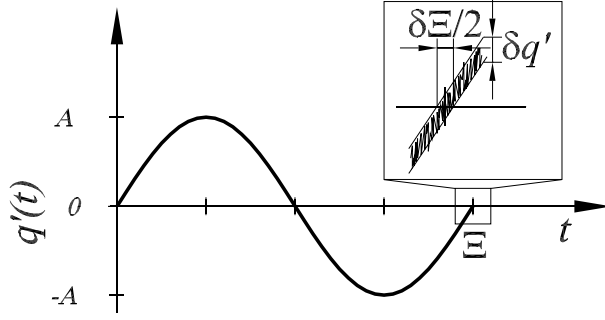


Figure 6.2: Typical cantilever deflection signal as it appears on an oscilloscope. The oscillation frequency is given by the inverse time lag between two consecutive zero-crossings with positive velocity.

deflection noise and the slope of the $q'(t)$ curve:

$$\frac{\delta \Xi}{2} = \frac{\delta q'}{2\pi f_0 A}. \quad (6.2)$$

Because $f_0 = 1/\Xi$, $\delta f_0/f_0 = \delta \Xi/\Xi$ and

$$\frac{\delta f_0}{f_0} = \frac{\delta q'}{\pi A}. \quad (6.3)$$

Thus, the frequency noise is proportional to the deflection noise and inversely proportional to the amplitude.

The thermal fluctuation of the cantilever deflection is calculated using the equipartition theorem, which states that the thermal energy stored in the cantilever per degree of freedom at temperature T is $k_B T/2$. The effect of the thermal contact between the cantilever and a reservoir at temperature T is that the cantilever is subject to thermal kicks such that its mean thermal energy $k A_{rms}^2$ equals $k_B T$. Because the thermal kicks are random, their frequency spectrum is white. \hat{A}_{drive} and its magnitude can be calculated by integrating the square of Eq. 4.3 from $f_{drive} = 0$ to $f_{drive} = \infty$ and setting $A_{drive} = \hat{A}_{drive}$ [4, 16]. The rms driving amplitude density (unit $\text{m}/\sqrt{\text{Hz}}$) is then given by:

$$\hat{A}_{drive} = \sqrt{\frac{2k_B T}{\pi k f_0 Q}}. \quad (6.4)$$

The response of the cantilever for frequencies much smaller than its eigenfrequency is unity (see Eq. 4.3), therefore an estimate of the thermal deflection noise is given by

the square root of the integral of the squared driving amplitude over the measurement bandwidth B :

$$\delta q' = \sqrt{\frac{2k_B T B}{\pi k f_0 Q}}. \quad (6.5)$$

The relative frequency noise is then given by

$$\frac{\delta f_0}{f_0} = \sqrt{\frac{2k_B T B}{\pi^3 k A^2 f_0 Q}} \quad (6.6)$$

which is similar to the expressions found by Martin *et al.* [71] and Albrecht *et al.* [4].

Equation 6.6 is a lower threshold for the noise in the frequency shift measurement which is caused by fundamental thermodynamic reasons. In practice, the instrumental noise in the measurement of q' can exceed this lower limit by orders of magnitude. For example, typical vertical resolutions of commercial AFMs are of the order of 0.1 \AA deflection over a bandwidth of 100 Hz, yielding an experimental deflection noise density of $1 \text{ pm}/\sqrt{\text{Hz}}$, while the thermal limit, according to Eq. 6.4 is $9 \text{ fm}/\sqrt{\text{Hz}}$ for $f_0 = 100 \text{ kHz}$, $k = 1 \text{ N/m}$ and $Q = 300$. For the qPlus sensor introduced in the next chapter, the experimental deflection noise density is $80 \text{ fm}/\sqrt{\text{Hz}}$, while the thermal limit is $0.14 \text{ fm}/\sqrt{\text{Hz}}$ for the typical qPlus parameters of $f_0 = 20 \text{ kHz}$, $k = 1800 \text{ N/m}$ and $Q = 4000$.

Equation 6.6 shows that the noise in the frequency measurement can be decreased by decreasing the detection bandwidth B . However, a low detection bandwidth limits the maximum imaging speed, and very slow imaging speeds at room temperature increase distortions in the images caused by lateral thermal drift between tip and sample. If a section with a width of 100 atoms is to be imaged at an imaging speed of three lines per second, B needs to be at least $2 \times 100 \times 3/\text{s} = 600 \text{ Hz}$. When working at room temperature, a lateral drift of the tip versus the sample is usually experienced at a rate of a few \AA per minute. Therefore, a scanning speed of a few lines per second is typically required in order to obtain images with little distortions. At low temperature, where thermal drift is negligible, the scanning speed can be set to very small values. With a low-temperature AFM, Lantz and coworkers reduced the scanning speed to as little as 0.063 lines per second [66]. The bandwidth B can be reduced significantly, which decreases the noise level.

The use of cantilevers with high Q also helps to reduce the frequency noise (Eq. 6.6). However, Eq. 4.8 and the discussion on page 28 imply that Q should not be

significantly larger than the ratio between the energy stored in the cantilever and the energy loss per oscillation cycle due to the tip-sample interaction. If Q is much higher than this value, controlling the amplitude of the cantilever can become difficult and instabilities are likely to occur.

6.2.2 Drifts of the eigenfrequency

The low frequency noise of the cantilever deflection can be filtered by the bandpass filter (see Fig. 4.1). However, drifts in f_0 on a slower time scale show up as a low frequency noise in the frequency shift signal. This drift can be caused by changes in temperature. The eigenfrequency (see Eq. 5.3) is determined by the spring constant and the effective mass of the cantilever. The spring constant changes with temperature, due to thermal expansion and the change of Young's modulus E_Y with temperature. Changes of the effective mass due to picking up a few atoms from the sample or transferring some atoms from the tip to the sample are insignificant, because a typical cantilever contains at least 10^{14} atoms. The resonance frequency of a cantilever is given in Eq. 2.13. With the velocity of sound in the cantilever material $v_s = \sqrt{E_Y/\rho}$, Eq. 2.13 can be expressed as [24]:

$$f_0 = 0.162v_s \frac{t}{L^2}. \quad (6.7)$$

The temperature dependence of the eigenfrequency is then given by

$$\frac{1}{f_0} \frac{\partial f_0}{\partial T} = \frac{1}{v_s} \frac{\partial v_s}{\partial T} - \alpha \quad (6.8)$$

where α is the thermal expansion coefficient. For silicon along the [110]-crystal direction (see Fig. 2.6 on page 15), $\frac{1}{v_s} \frac{\partial v_s}{\partial T} = -5.5 \times 10^{-5} K^{-1}$ and $\alpha = 2.55 \times 10^{-6} K^{-1}$ at $T = 290$ K [64, 65]. The resulting relative frequency shift for (rectangular) silicon cantilevers is then $-5.8 \times 10^{-5} K^{-1}$. This is a large noise source in classical FM-AFM, where relative frequency shifts can be as small as $-6 \text{ Hz}/151\text{kHz} = -4 \times 10^{-5}$ (see row 5 in Table 4.1) and a temperature variation of $\Delta T = +0.69$ K causes an equal shift in resonance frequency. The drift of f_0 with temperature is much smaller for cantilevers made of quartz, as shown in the next chapter.

Less significant noise sources, like the thermal fluctuation of A , are discussed in Ref. [A6].

6.3 Optimal amplitude for minimal vertical noise

The total vertical noise is given by the ratio of the frequency noise and the slope of the frequency shift versus distance curve. Both the nominator and denominator are functions of the amplitude – the frequency noise is proportional to $1/A$, the slope of the frequency shift curve is constant at first and drops as $A^{-1.5}$ for large amplitudes [A4]. Thus, there is a minimal noise for amplitudes in the order of the range λ of the tip sample force F_{ts} [A6]:

$$A_{optimal} \approx \lambda. \quad (6.9)$$

For chemical forces, $\lambda \approx 1 \text{ \AA}$. However, operating a conventional cantilever with amplitudes in the \AA -range close to a sample is in general impossible because of the jump-to-contact problem (section 3.1). The cantilever spring constant k needs to be at least a few hundred N/m to enable operation with amplitudes in the \AA -range.

Chapter 7

A novel force sensor based on a quartz tuning fork

7.1 Quartz versus silicon as a cantilever material

Cantilevers for AFM are small devices and are therefore not machined with traditional manufacturing techniques like grinding and milling, but by photolithography. Photolithography works for both quartz and silicon. Cantilevers should also have a high Q -factor, thus the material should have little internal dissipation. This condition is fulfilled both for single-crystal silicon and quartz. It was shown in section 6.2 that thermal drifts of the eigenfrequency of the force sensor show up as noise in FM-AFM. In this respect, quartz is clearly superior to silicon, as quartz can be cut along certain crystal orientations such that the variation of oscillation frequency of a tuning fork is zero for a certain temperature $T_{ambient} \approx 296$ K [72]. This cannot be accomplished with silicon cantilevers. Figure 7.1 shows a comparison of typical frequency variations as a function of temperature for silicon and quartz. The data for silicon is calculated in Eq. 6.8, the quartz data is taken from Ref. [72]. As can be seen, quartz is remarkably stable at room temperature compared to silicon. A very appealing property of quartz as a sensor material is its piezoelectricity, which allows the construction of self-sensing devices. The deflection of silicon cantilevers is most commonly measured by optical detection through an interferometer or by bouncing a light beam off the cantilever and measuring its deflection (“beam bounce method”). For detailed descriptions of these techniques, see Ref. [88]. Self sensing piezoresistive sensors [100] have also been quite successful – the first AFM image of silicon with

atomic resolution was achieved with a piezoresistive cantilever [A2]. Piezoelectric sensors based on thin films of materials with much higher piezoelectric constants than quartz [56] are also available. However, these devices lack the very low internal dissipation and high frequency stability of quartz. The general advantage of piezoelectric sensors versus piezoresistive sensors is that the latter dissipate power in the mW range, while electric dissipation is negligible in piezoelectric sensors. Therefore, piezoelectric sensors are preferred for low temperature applications.

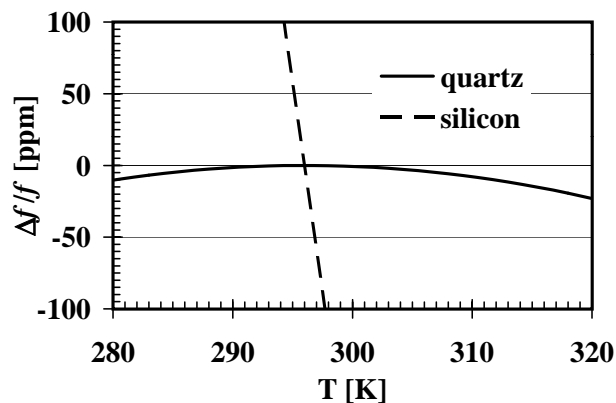


Figure 7.1: Plot of frequency variation as a function of temperature.

7.2 Previous applications of tuning forks in scanning probe microscopy

The problem of establishing a constant frequency standard has been around for centuries in the pursuit of increasing the accuracy of timepieces. The seventies brought about a revolution with the introduction of quartz tuning forks as frequency standards in clocks [72, 104]. Billions of these devices are now manufactured annually, and the deviations of even low cost watches are no more than a few seconds a week. Tuning forks made of quartz are cheap and amply available, and experimental studies of using them as force sensors were done soon after the invention of the AFM. Gthner *et al.* [46, 47] have used tuning forks as force sensors in acoustic near field microscopy and Karrai *et al.* [60] have used a tuning fork to control the distance between the optical near field probe and the surface in a scanning near-field-optical

microscope. Rychen *et al.* have demonstrated the use of quartz tuning forks at low temperature [87] and other applications of quartz tuning forks as force sensors can be found in Refs. [32, 84, 85, 101, 102, 105].

In spite of all the advantages of tuning forks, a decisive disadvantage of them is that a force sensing cantilever should only have one beam, and a tuning fork necessarily has two coupled beams. This problem can be avoided by fixing one of the two beams, as shown in the next section.

7.3 Benefit of clamping one of the beams (qPlus configuration)

Figure 7.2 shows a mechanical equivalent of a tuning fork. In a quartz tuning fork pro-

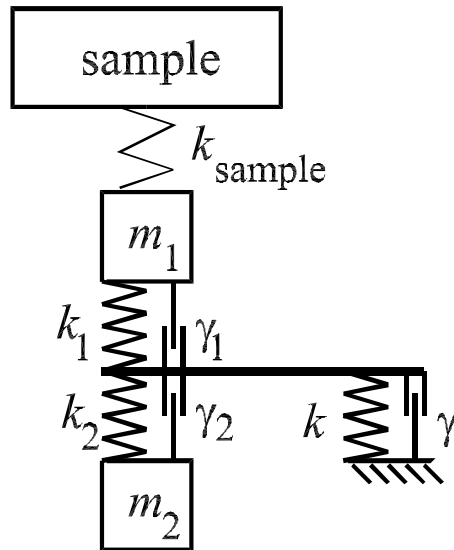


Figure 7.2: Mechanical equivalent of a tuning fork.

duced for watch applications, k_1 and k_2 are equal and m_1 and m_2 are laser trimmed individually by evaporating a gold plating at the ends of the beams. By laser trimming, the eigenfrequency of each beam is adjusted to f_0 . For most tuning forks built for watch applications $f_0 = 2^{15} \text{ Hz} = 32768 \text{ Hz}$. When both beams are equal in their masses and spring constants, an oscillation mode with extremely little damping exists where the beams oscillate opposite to each other. The dynamical forces of the

two beams are then compensated in the base part, and the mechanical properties of the mount (k and γ) are irrelevant. Because the base part and beams are made out of single quartz crystal, internal dissipation is low in this oscillation mode and the Q -value is extremely high (up to 100000 in vacuum and 10000 in air). In all the applications listed in the previous section, the fork is mounted in the same way as in a watch, i.e. it is fixed at the base part. However, the symmetry of the beams is broken when a tip is mounted to one of them. This asymmetry can be cured by mounting a counterweight on the other beam, as described in a patent by Dransfeld et al. [28]. However, when the tip is subject to a tip sample interaction, the asymmetry cannot be restored in this manner. Even conservative tip sample forces (i.e. no hysteresis in the $F_{ts}(z)$ -curve) cause damping in this mode, only slow scanning speeds are possible and the imaging signal is very difficult to interpret.

Fixing one of the beams firmly to a supporting structure overcomes this problem. Because Q does not drop for conservative tip-sample forces in this configuration, this device has been named “qPlus-sensor” [41].

The first prototype of this device used a tuning fork with a spring constant of $k = 3140$ N/m and a piece of pyrex glass as a substrate for the fixed beam (see Fig. 1 in Ref. [A5]). Initial tests of the device were conducted on compact discs and test gratings in ambient conditions [A5]. The device was improved by designing a custom alumina substrate and using different tuning forks with spring constants of $k = 1800$ N/m (see Fig. 1 in Ref. [A8]). Also, the preamplifier was improved.

The supreme noise performance of the sensor that was predicted theoretically in the preceding chapters, has been verified experimentally by the achievement of a breakthrough in AFM resolution [A9] – the observation of subatomic features in real space for the first time.

Recently, a patent for the qPlus sensor has been issued [41].

Chapter 8

Summary and Outlook

The essence of the work presented here is the introduction, the advance in theoretical understanding and the practical improvement of frequency-modulation AFM as a viable technique that enriches the toolset of surface scientists. In the course of this work, true atomic resolution by AFM on a reactive surface has been demonstrated for the first time, the theoretical understanding of the origin of frequency shifts in FM-AFM has been advanced, the theoretical comprehension of the instrumental noise limit has been extended, an easy-to-use force sensor with unprecedented resolution has been introduced and subatomic features of an atom (see Fig. 8.1) have been observed for the first time in real space [A9]. Figure 8.1 is an image of a single silicon

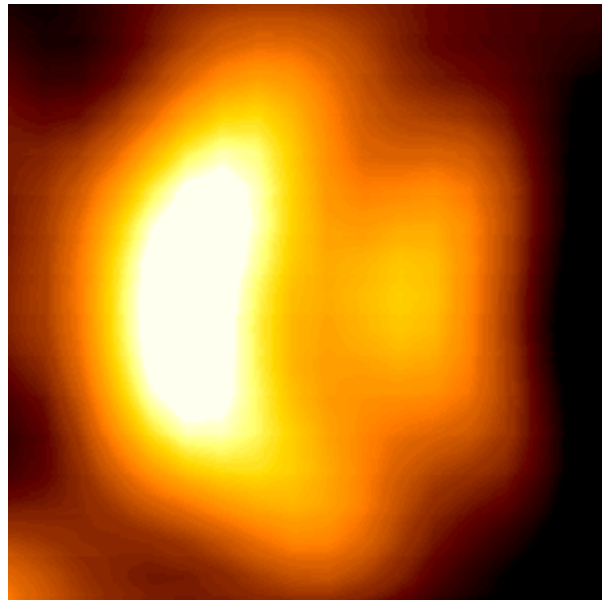


Figure 8.1: Image of a single atom. Image size: 6.6 Å lateral, 1.4 Å vertical.

adatom. Silicon adatoms display a single sp^3 dangling bond sticking out perpendicular from the surface. Thus, the image of this atom is expected to be spherically symmetric with respect to the vertical axis. We interpret the image as being caused by an overlap of two sp^3 dangling bonds from the tip with the single dangling bond from the surface, for a detailed description see Refs. [A9, 42]. On the subatomic level, the image is sensitive to the chemical identity and the structural surroundings of the front atom of the tip. First attempts to engineer tips with a known symmetry are under way [A10].

Nevertheless, there are more opportunities to come.

Many of the open questions and future applications are listed as topics for the Forth International Conference on Noncontact Atomic Force Microscopy which will take place from September 2 - 5 2001 in Kyoto, Japan and can be divided into experimental, theory and instrumentation issues.

- Experimental challenges
 1. Utilisation of FM-AFM on more and new sample materials (semiconductors, metals, insulators, ferromagnetic-, ferroelectric-, biological materials).
 2. Atomic manipulation, like demonstrated with an STM by Eigler *et al.* [33], could also be undertaken by AFM. Because the STM only works on conductive surfaces, the assembly of metallic atoms on isolating substrates is not possible by STM. If atoms could be manipulated on isolating substrates, it is conceivable to build electronic devices from single atoms.
 3. Three dimensional mapping of atomic force with atomic resolution is technically possible by FM-AFM by oscillating the cantilever parallel to the surface.
 4. Quantitative measurements of damping with atomic resolution.
 5. Combined STM and AFM measurements where tunneling current, frequency shift and dissipation are measured simultaneously with atomic resolution.
- Theoretical challenges

1. Dissipation – the force laws between individual atoms are conservative, it is not clear how dissipation and friction originate on an atomic level. Studies of dissipation on the atomic level are possible by FM-AFM and are also a very interesting application.
 2. Angular dependence of tip-sample force.
- Instrumentation issues
 1. Force sensors (functionalized tips, optimal stiffness, high stability in f_0 , lateral forces).
 2. Control electronics (frequency detector, oscillator electronics, non-linear feedback).

This summary of challenges shows that AFM with true atomic resolution is presently opening exciting possibilities in nanoscience. Nanoscience has been identified to be a key for the next breakthroughs in physics, chemistry and biology that are the basis for future innovations in technology. AFM with atomic resolution will play an important role in this venture, because it grants access to the very scaffolding of matter: the chemical bond.

Chapter 9

Bibliography

- [1] M. Abramowitz, I. Stegun, *Handbook of Mathematical Functions*, 9th ed., (Dover Publications, New York 1970).
- [2] S. Akamine, R.C. Barrett, C.F. Quate, *Appl. Phys. Lett.* **57**, 316 (1990).
- [3] T.R. Albrecht, S. Akamine, T.E. Carver, C.F. Quate, *J. Vac. Sci. Technol. A* **8**, 3386 (1990).
- [4] T.R. Albrecht, P. Grütter, D. Horne, D. Rugar, *J. Appl. Phys.* **69**, 668 (1991).
- [5] T.R. Albrecht, private communication (2000).
- [6] W. Allers, A. Schwarz, U.D. Schwarz, R. Wiesendanger, *Rev. Sci. Instrum.* **69**, 221 (1998).
- [7] W. Allers, A. Schwarz, U.D. Schwarz, R. Wiesendanger, *Appl. Surf. Sci.* **140**, 247 (1999).
- [8] W. Allers, A. Schwarz, U.D. Schwarz and R. Wiesendanger, *Europhys. Lett.* **48**, 276 (1999).
- [9] Analog Devices Inc., One Technology Way, P.O.B. 9106, Norwood, MA 02062, USA.
- [10] B. Anczykowski, B. Gotsmann, H. Fuchs, J.P. Cleveland, V.B. Elings, *Appl. Surf. Sci.* **140**, 376 (1999).
- [11] B. Anczykowski, D. Krüger, H. Fuchs, *Phys. Rev. B* **53**, 15485 (1996).

- [12] N. Ashcroft, N.D. Mermin, *Solid State Physics*, p. 398 (Saunders College, Philadelphia 1981).
- [13] M. Bammerlin, R. Lüthi, E. Meyer, A. Baratoff, J. Lü, M. Guggisberg, Ch. Gerber, L. Howald, H.J. Güntherodt, *Probe Microscopy* **1**, 3 (1997).
- [14] A. Baratoff (unpublished).
- [15] G. Baym, *Lectures on Quantum Mechanics*, (Benjamin New York 1969).
- [16] R. Becker, *Theorie der Wärme*, 3rd ed., p. 303 (Springer Berlin New York 1985).
- [17] H. Bielefeldt, F.J. Giessibl, *Surface Science* **440**, L863 (1999).
- [18] G. Binnig, H. Rohrer, Ch. Gerber, E. Weibel, *Phys. Rev. Lett.* **49**, 57 (1982).
- [19] G. Binnig, H. Rohrer, Ch. Gerber, E. Weibel, *Phys. Rev. Lett.* **50**, 120 (1983).
- [20] G.K. Binnig, H. Rohrer, *Scientific American* **10**, 74 (1984).
- [21] G. Binnig, C.F. Quate and Ch. Gerber, *Phys. Rev. Lett.* **56**, 930 (1986).
- [22] G. Binnig, H. Rohrer, *Rev. Mod. Phys. A* **7**, S325 (1999).
- [23] N. Burnham, R.J. Colton, *J. Vac. Sci. Technol. A* **7**, 2906 (1989).
- [24] C.J. Chen, *Introduction to Scanning Tunneling Microscopy*, (Oxford University Press, New York 1993).
- [25] S. Ciraci, A. Baratoff, Inder P. Batra, *Phys. Rev. B* **41**, 2763 (1990).
- [26] C.A. Coulson, R. McWeeny, *Coulson's Valence*, 3rd ed., (Oxford University Press, Oxford 1991).
- [27] M.F. Crommie, C.P. Lutz, D.M. Eigler, *Science* **262**, 218 (1993).
- [28] K. Dransfeld, U. Fischer, P. Güthner, K. Heitmann, US Patent 5212987 (1991).
- [29] U. Dürig, *Surf. and Interf. Anal. SIA* **27**, 467 (1999).
- [30] U. Dürig, *Appl. Phys. Lett.* **75**, 433 (1999).

- [31] U. Dürig, *New Journal of Physics* **2**, 5.1-5.12 (2000).
- [32] H. Edwards, L. Taylor, W. Duncan and A. Melmed, *J. Appl. Phys.* **82**, 980 (1997).
- [33] D.M. Eigler, E.K. Schweizer, *Nature* **344**, 524 (1990).
- [34] R. Erlandsson, L. Olsson, P. Martensson, *Phys. Rev. B* **54**, R8309 (1996).
- [35] K. Fukui, H. Onishi, Y. Iwasawa, *Phys. Rev. Lett.* **79**, 4202 (1997).
- [36] F.J. Giessibl, Ch. Gerber, G. Binnig, *J. Vac. Sci. Technol. B* **9**, 984 (1991).
- [37] F.J. Giessibl, *PhD thesis*, LMU München, Germany (1991).
- [38] F.J. Giessibl, *Phys. Rev. B* **45**, 13815 (1992).
- [39] F.J. Giessibl, G. Binnig, *Ultramicroscopy* **42-44**, 281 (1992).
- [40] F.J. Giessibl, *Jpn. J. Appl. Phys.* **33**, 3726 (1994).
- [41] F.J. Giessibl, Patent DE 196 33 546, German Patent Office (1996).
- [42] F.J. Giessibl, *Spektrum der Wissenschaft* (in press).
- [43] H. Goldstein, *Classical Mechanics* (Addison Wesley, Reading MA 1980).
- [44] B. Gotsmann, C. Schmidt, C. Seidel, H. Fuchs, *Eur. Phys. J. B* **4**, 267 (1998).
- [45] H.-J. Güntherodt, R. Wiesendanger (Eds.), *Scanning tunneling microscopy I-III* (Springer Verlag Berlin Heidelberg 1991).
- [46] P. Güthner, U. Fischer, K. Dransfeld, *Appl. Phys. B* **48**, 89 (1989).
- [47] P. Güthner, Dissertation University Konstanz, Germany (1992).
- [48] P. Güthner, *J. Vac. Sci. Technol. B* **14**, 2428 (1996).
- [49] H.C. Hamaker, *Physica* **4**, 1058 (1937).
- [50] U. Hartmann, *J. Vac. Sci. Technol. B* **9**, 465 (1991).
- [51] H. Hölscher, U.D. Schwarz, R. Wiesendanger, *Appl. Surf. Sci.* **140**, 344(1999).

- [52] P. Horowitz, W. Hill, *The Art of Electronics*, 2nd ed., (Cambridge University Press, Cambridge, New York 1989).
- [53] L. Howald, R. Lüthi, E. Meyer, P. Güthner, H.-J. Güntherodt, *Z. Phys. B* **93**, 267 (1994).
- [54] L. Howald, R. Lüthi, E. Meyer, H.-J. Güntherodt, *Phys. Rev. B* **51**, 5484 (1995).
- [55] J. Israelachvili, *Intermolecular and Surface Forces*, 2nd ed., (Academic Press, London 1991).
- [56] T. Itoh and T. Suga, *Nanotechnology* **4**, 218 (1993).
- [57] S.P. Jarvis, H. Yamada, S.-I. Yamamoto, H. Tokumoto, J. B. Pethica, *Nature* **384**, 247 (1996).
- [58] S.P. Jarvis, S.-I. Yamamoto, H. Yamada, H. Tokumoto, J. B. Pethica, *Appl. Phys. Lett.* **70**, 2238 (1997).
- [59] JSPM-4500, JEOL Ltd., 1-2 Musashino 3-chome Akishima Tokyo, Japan.
- [60] K. Karrai, R. D. Grober, *Appl. Phys. Lett.* **66**, 1842 (1995).
- [61] S. Kitamura, M. Iwatsuki, *Jpn. J. Appl. Phys.* **34**, L145 (1995).
- [62] S. Kitamura, M. Iwatsuki, *Jpn. J. Appl. Phys.* **35**, L668 (1996).
- [63] H. Krupp, *Advances Colloid Interface Sci.* **1**, 113 (1967).
- [64] H. Kuchling, *Taschenbuch der Physik* (Harri Deutsch, Thun and Frankfurt/Main 1982).
- [65] Landolt-Börnstein, *Numerical Data and Functional Relationships in Science and Technology, Vol. 17a*, edited by O. Madelung, M. Schultz and H. Weiss (Springer, Berlin 1982).
- [66] M.A. Lantz, H.J. Hug, P.J.A. von Schendel, R. Hoffmann, S. Martin, A. Baratoff, A. Abdurixit, H.-J. Güntherodt, Ch. Gerber, *Phys. Rev. Lett.* **84**, 2642 (2000).

- [67] A.I. Livshits, A.L. Shluger, A.L. Rohl, A.S. Foster, *Phys. Rev. B* **59**, 2436 (1999).
- [68] Ch. Loppacher et al., *Appl. Surf. Sci.* **140**, 287 (1999).
- [69] R. Lüthi, E. Meyer, M. Bammerlin, A. Baratoff, T. Lehmann, L. Howald, Ch. Gerber, H.J. Güntherodt, *Z. Phys. B* **100**, 165 (1996).
- [70] H.C. Manoharan, C.P. Lutz, D.M. Eigler, *Nature* **403**, 512 (2000).
- [71] Y. Martin, C.C. Williams, H.K. Wickramasinghe, *J. Appl. Phys.* **61**, 4723 (1987).
- [72] E. Momosaki, *Proc. 1997 IEEE Internatl. Freq. Contr. Symp.*, 552 (1997).
- [73] Nanosurf AG, Liestal, Switzerland.
- [74] F. Ohnesorge, G. Binnig, *Science* **260**, 1451 (1993).
- [75] Omicron UHV AFM/STM, Omicron Vakuumphysik GmbH, Taunusstein, Germany.
- [76] S. Orisaka *et al.*, *Appl. Surf. Sci.* **140**, 243 (1999).
- [77] J. Patrin, presentation at STM 95 (Aspen, Colorado 1995).
- [78] L. Pauling, *The Nature of the Chemical Bond*, 2nd ed., (Cornell Univ. Press, Ithaca, N.Y. 1957).
- [79] R. Perez, I. Stich, M.C. Payne, K. Terakura, *Phys. Rev. Lett.* **78**, 678 (1997).
- [80] R. Perez, I. Stich, M.C. Payne, K. Terakura, *Phys. Rev. B* **58**, 10835 (1998).
- [81] J. Pethica, *Phys. Rev. Lett.* **57**, 3235 (1986).
- [82] H. Raza, C.L. Pang, S.A. Haycock, G. Thornton, *Phys. Rev. Lett.* **82**, 5265 (1999).
- [83] M. Reichling and C. Barth, *Phys. Rev. Lett.* **83**, 768 (1999).
- [84] W.H.J. Rensen, N.F. van der Hulst, A.G.T. Ruiter, P.E. West, *Appl. Phys. Lett.* **75**, 1640 (1999).

- [85] A.G.T. Ruiter, J.A. Veerman, K.O. van der Werf, N.F. van Hulst, *Appl. Phys. Lett.* **71**, 28 (1997).
- [86] D. Rugar and P. Hansma, *Physics Today*, October 1990, 23 (1990).
- [87] J. Rychen, T. Ihn, P. Studerus, A. Herrmann, K. Ensslin, *Rev. Sci. Instr.* **70**, 2765 (1999).
- [88] D. Sarid, *Scanning Force Microscopy*, (Oxford University Press, New York 1994).
- [89] N. Sasaki, M. Tsukada, *Jpn. J. Appl. Phys.* **37**, L533 (1998).
- [90] N. Sasaki, M. Tsukada, *Appl. Surf. Sci.* **140**, 339 (1999).
- [91] N. Sasaki, M. Tsukada, *Jpn. J. Appl. Phys.* **37**, L533 (1998); *Appl. Surf. Sci.* **140**, 339 (1999).
- [92] A. Schwarz, W. Allers, U.D. Schwarz, R. Wiesendanger, *Appl. Surf. Sci.* **140**, 299 (1999).
- [93] I.Yu. Sokolov, G.S. Henderson, F.J. Wicks, *Appl. Surf. Sci.* **140**, 362 (1999).
- [94] F.H. Stillinger, T.A. Weber, *Phys. Rev. B* **31**, 5262 (1985).
- [95] J.A. Stroscio, W.J. Kaiser (Eds.), *Scanning tunneling microscopy* (Academic Press Boston 1993).
- [96] Y. Sugawara, M. Ohta, H. Ueyama, S. Morita, *Science* **270**, 1648 (1995).
- [97] Y. Sugawara, H. Ueyama, T. Uchihashi, M. Ohta, Y. Yanase, T. Shigematsu, M. Suzuki, S. Morita, Materials Research Society 1996 Fall Meeting, Proceedings E: Defects in Electric Materials II, Editors: J. Michel, T. Kennedy, K. Wada and K. Thonke, p. 16 (Boston, December 1996).
- [98] D. Tabor, R.H.S. Winterton, *Proc. R. Soc. London A* **312**, 435 (1969).
- [99] AutoProbe VP, ThermoMicroscopes, Sunnyvale, California, USA.
- [100] M. Tortonese, R.C. Barrett and C.F. Quate, *Appl. Phys. Lett.* **62**, 834 (1993).

- [101] M. Todorovic, S. Schulz, *J. Appl. Phys.* **83**, 6229 (1998).
- [102] D.P. Tsai, Y.Y. Lu, *Appl. Phys. Lett.* **73**, 2724 (1998).
- [103] H. Ueyama, Y. Sugawara, S. Morita, *Appl. Phys. A* **66**, S295 (1998).
- [104] F.L. Walls, p. 276 in E.A. Gerber and A. Ballato (Eds.) *Precision Frequency Control*, Academic Press, Orlando a.o. (1985).
- [105] L. Wang, *Appl. Phys. Lett.* **73**, 3781 (1998).
- [106] H.K. Wickramasinghe, *Scientific American* **10**, 74 (1989).
- [107] J.B.P. Williamson, *Proc. Inst. Mech. Eng.* **182**, 21 (1967).
- [108] R. Wiesendanger, *Scanning Probe Microscopy and Spectroscopy: Methods and Applications* (Cambridge University Press 1994).
- [109] R. Wiesendanger (Ed.), *Scanning Probe Microscopy: Analytical Methods* (Springer Verlag Berlin Heidelberg 1998).
- [110] J. Wintterlin, J. Wiechers, H. Brune, T. Gritsch, H. Höfer and R. J. Behm, *Phys. Rev. Lett.* **62**, 59 (1989).
- [111] O. Wolter, Th. Bayer, J. Greschner, *J. Vac. Sci. Technol.* **9** (2), 1353 (1991).
- [112] Q. Zhong, D. Innis, K. Kjoller, V.B. Elings, *Surf. Sci. Lett.* **290**, L688 (1993).

Chapter 10

Appendix: Selection of previously published work

[A1] ‘Piezoresistive cantilevers utilized for scanning tunneling and scanning force microscopy in ultrahigh vacuum’

F.J. Giessibl, B.M. Trafas, *Rev. Sci. Instrum.* **65**, 1923-1929 (1994).

[A2] ‘Atomic resolution of the silicon (111)-(7×7) surface by atomic force microscopy’

F.J. Giessibl, *Science* **267**, 68-71 (1995).

[A3] ‘Self-oscillating mode for frequency modulation noncontact atomic force microscopy’

F.J. Giessibl, M. Tortonese, *Appl. Phys. Lett.* **70**, 2529-2631 (1997).

[A4] ‘Forces and frequency shifts in atomic-resolution dynamic force microscopy’

F.J. Giessibl, *Phys. Rev. B* **56**, 16010-16015 (1997).

[A5] ‘High-speed force sensor for force microscopy and profilometry utilizing a quartz tuning fork’

F.J. Giessibl, *Appl. Phys. Lett.* **73**, 3956-3958 (1998).

[A6] ‘Calculation of the optimal imaging parameters for frequency modulation atomic force microscopy’

F.J. Giessibl, H. Bielefeldt, S. Hembacher, J. Mannhart, *Appl. Surf. Sci.* **140**, 352-357 (1999).

- [A7] ‘*Physical interpretation of frequency-modulation atomic force microscopy*’
F.J. Giessibl, H. Bielefeldt, *Phys. Rev. B* **61**, 9968-9971 (2000).
- [A8] ‘*Atomic resolution on Si (111)-(7×7) by noncontact atomic force microscopy with a force sensor based on a quartz tuning fork*’
F.J. Giessibl, *Appl. Phys. Lett.* **76**, 1470-1472 (2000).
- [A9] ‘*Subatomic features on the silicon (111)-(7×7) surface observed by atomic force microscopy*’
F.J. Giessibl, S. Hembacher, H. Bielefeldt, J. Mannhart, *Science* **289**, 422-425 (2000).
- [A10] ‘*Imaging silicon with crystallographically oriented tips by atomic force microscopy*’
F.J. Giessibl, S. Hembacher, H. Bielefeldt, J. Mannhart, *Proceedings NCAFM 2000, Appl. Phys. A* **71**, S15-S17 (2001).
- [A11] ‘*A direct method to calculate tip-sample forces from frequency shifts in frequency-modulation atomic force microscopy*’
F.J. Giessibl, *Appl. Phys. Lett.* **78**, 123-125 (2001).